



Revisiting the 1992 Landers earthquake: a Bayesian exploration of co-seismic slip and off-fault damage

Journal:	<i>Geophysical Journal International</i>
Manuscript ID	GJI-S-17-0463
Manuscript Type:	Research Paper
Date Submitted by the Author:	23-May-2017
Complete List of Authors:	Gombert, Baptiste; Institut de physique du globe de Strasbourg Duputel, Zacharie; Université de Strasbourg and EOST/CNRS UMR 7516, Institut de Physique du Globe de Strasbourg Jolivet, Romain; Ecole Normale Supérieure, Department of Geosciences Dubre, Cécile; Institut de physique du globe de Strasbourg Rivera, Luis; Institut de physique du globe de Strasbourg Simons, Mark; California Institute of Technology, Seismological Laboratory, Division of Geological and Planetary Sciences
Keywords:	Inverse theory < GEOPHYSICAL METHODS, Probability distributions < GEOPHYSICAL METHODS, Earthquake source observations < SEISMOLOGY, Fractures, faults, and high strain deformation zones < TECTONOPHYSICS

SCHOLARONE™
Manuscripts

1 submitted to *Geophys. J. Int.*
2
3
4
5
6

7 Revisiting the 1992 Landers earthquake: a Bayesian 8 9 exploration of co-seismic slip and off-fault damage 10 11

12
13
14
15 B. Gombert¹, Z. Duputel¹, R. Jolivet², C. Doubre¹, L. Rivera¹ and M. Simons³
16
17

18¹ *Institut de Physique du Globe de Strasbourg, UMR7516, Université de Strasbourg, EOST/CNRS*
19
20

21² *Laboratoire de géologie, Département de Géosciences, École Normale Supérieure,
22
23 PSL Research University, CNRS UMR, Paris, France*

24³ *Seismological Laboratory, Geological and Planetary Sciences, California Institute of Technology,
25
26 Pasadena, California, USA*
27
28

33 Received XX; in original form XX
34
35
36

37 SUMMARY 38 39

40
41
42 Existing models for the distribution of subsurface fault slip associated with the 1992 Landers
43
44 (CA) earthquake ($M_w = 7.3$) show significant dissimilarities. In particular, they exhibit differ-
45
46 ent amounts of slip at shallow depths (< 5km). These discrepancies can be primarily attributed
47
48 to the ill-posed nature of the slip inversion problem and to the use of physically unjustifiable
49
50 smoothing or regularization constraints. In this study, we propose a new coseismic model ob-
51
52 tained from the joint inversion of multiple observations in a relatively unregularized and fully
53
54 Bayesian framework. We use a comprehensive dataset including GPS, terrestrial geodesy, mul-
55
56
57
58
59
60

1 2 *B. Gombert*

2
3 10 tiple SAR interferograms and co-seismic offsets from correlation of aerial images. These ob-
4
5 11 servations provide dense coverage of both near- and far-field deformation. To limit the impact
6
7 12 of modeling uncertainties, we develop a 3D fault geometry designed from field observations,
8
9 13 co-seismic offsets and the distribution of aftershocks. In addition, we account for uncertainty in
10
11 14 the assumed elastic structure used to compute the Greens functions. Our solution includes the
12
13 15 ensemble of all plausible models that are consistent with our prior information and fit the avail-
14
15 16 able observations within data and prediction uncertainties. Using near-fault high-resolution
16
17 17 ground deformation measurements and the density of aftershocks, we investigate the proper-
18
19 18 ties of the damage zone and its impact on the inferred slip at depth. We attribute a part of the
20
21 19 inferred slip deficit at shallow depth to our models not including the impact of a damage zone
22
23 20 associated with a reduction of shear modulus in the vicinity of the fault.

24
25 21 **Key words:** Inverse theory; Probability distributions; Earthquake source observations; Frac-
26
27 22 tures, faults, and high strain deformation zones

36 23 1 INTRODUCTION

37
38
39 24 Following the 1979 Imperial Valley earthquake more than three decades ago (Olson & Apsel 1982,
40
41 25 Hartzell & Heaton 1983), finite-fault source models have been routinely constructed after most
42
43 26 significant earthquakes. Despite the increasing volume and quality of available geodetic and seis-
44
45 27 mological data, we still observe a significant variability in inferred subsurface fault slip for any
46
47 28 given event. Estimating the distribution of fault slip from surface deformation is fundamentally an
48
49 29 ill-posed inverse problem with different models that can fit the data equally well. Furthermore, data
50
51 30 and forward predictions are imperfect and the corresponding uncertainties are often difficult to ac-
52
53 31 count for. A standard approach to overcome the non-uniqueness of the solution relies on Tikhonov

A Bayesian exploration of the Landers Earthquake 3

regularization (e.g. Hansen 1998) involving minimization of first or second order spatial derivatives of the slip model to enforce smoothness of the slip distribution. However, such regularization is not physically justifiable, with the choice of damping potentially having a dramatic effect on the solution. The impact of different approaches to regularization, coupled with the lack of consideration of model uncertainties, can hamper our ability to draw clear conclusions about earthquake source processes.

Due to the availability of a comprehensive dataset, many finite-fault models have been published for the 1992 $M_w = 7.3$ Landers earthquake (e.g., Murray et al. 1993, Cohee & Beroza 1994, Hudnut et al. 1994, Freymueller et al. 1994, Wald & Heaton 1994, Cotton & Campillo 1995, Fialko 2004b, Xu et al. 2016). Common patterns emerge in the inferred slip distributions including the fact that most of the slip occurred in the central section of the rupture (i.e., the Homestead Valley Fault). However, there are also clear inconsistencies. In particular, the extent of shallow slip significantly varies between models (from 6% to 46%). Since there is no indication of large inter- or post-seismic slip at shallow depth, the amount of such co-seismic slip deficit has an impact on seismic risk assessment as this suggests that part of the accumulated strain is not released by the earthquake (Simons et al. 2002, Fialko et al. 2005). Simons et al. (2002) and Kaneko & Fialko (2011) suggested that such deficits might be an artifact due to inelastic response of the medium in the vicinity of the fault. Anelasticity would bias slip models where observations at short distances are modeled assuming elastic Green's functions. An apparent shallow slip deficit could also be caused by smoothing constraints and sparseness of near-fault data (Simons et al. 2002, Xu et al. 2016). Finally, unaccounted heterogeneities in the crust elastic properties can also result in a biased slip distribution at depth (Barbot et al. 2008).

1 4 *B. Gombert*

2
3 54 We perform a Bayesian exploration of the 1992 Landers rupture to evaluate the population
4
5 55 of plausible slip models given geodetic data and forward problem uncertainties. Our approach is
6
7 56 exempt from any smoothing and allows us to assess the extent of any purported shallow slip deficit
8
9 57 as constrained by available geodetic data. Using near-fault data, we also investigate the impact of
10
11 58 lateral heterogeneities on the inferred slip distribution at depth.

12
13 59 **2 DATA OVERVIEW**

14
15
16
17 60 We use a large geodetic dataset composed of GPS measurements at 82 sites, 23 trilateration mea-
18
19 61 surements, 2 SAR interferograms and 14 optical correlation images. This combination of data
20
21 62 provides good coverage in both the near- and far-fields.

22
23 63 **2.1 GPS and trilateration data**

24
25
26 64 We use 3-component observations from 82 GPS stations scattered across southern California (Hud-
27
28 65 nut et al. 1994) with a few stations in the vicinity of the fault (Figs 1(a) and 2). Observations of the
29
30 66 vertical component of displacement is associated with significantly larger uncertainties than the
31
32 67 horizontal components. In addition, a trilateration network covers the southern part of the rupture
33
34 68 (Figs 1(a) and 2). We invert directly the horizontal relative line-length changes provided by Murray
35
36 69 et al. (1993) instead of the pre-inverted displacement vectors of the trilateration stations. The GPS
37
38 70 and trilateration data include up to a few months of inter-seismic and post-seismic deformation.
39
40 71 However, the associated post-seismic displacements measured by GPS are expected to be less than
41
42 72 ~10 cm, which is substantially smaller than the ~8 m of co-seismic displacement observed near
43
44 73 the faults. (Murray et al. 1993, Peltzer et al. 1998).

1
2
3 **2.2 InSAR data**
4
5
6
7
8
9
10
11
12
13
14
15
16
17
18
19
20
21
22
23
24
25
26
27
28
29
30
31
32
33
34
35
36
37
38
39
40
41
42
43
44
45
46
47
48
49
50
51
52
53
54
55
56
57
58
59
50 We use two SAR interferograms computed from pre- and post-earthquake acquisitions on both as-
cending and descending tracks of the ERS satellite (Fig. 1(b) and (c)). Interferograms are computed
using the ROI_PAC software (Rosen et al. 2004). We downsample the unwrapped interferograms
using a recursive quad-tree algorithm (Simons et al. 2002, Lohman & Simons 2005) to reduce the
number of observation points. The final downsampled ascending and descending interferograms
contain 730 and 663 pixels, respectively. Using the procedure described by Jolivet et al. (2014)
for each InSAR scene, we estimate an empirical data covariance function, which statistically rep-
resents atmospheric noise. We find standard deviations of 3.5 cm and 0.9 cm for the descending
and ascending tracks, respectively. The correlation length is 11 km for both images. Covariance
functions are shown in Fig. S1 available in the electronic supplement. While the second image
of the interferogram on the ascending track was acquired only two days after the mainshock, the
interferogram on the descending track includes more than one month of post-seismic deformation.37
38 **2.3 Optical correlation images**
39
40
41
42
43
44
45
46
47
48
49
50
51
52
53
54
55
56
57
58
59
50 We use optical correlation images of the ground displacement from Ayoub et al. (2009). Maps of
ground displacement are made using 14 pairs of aerial photographs acquired before and after the
earthquake. Cross-correlation is performed to derive horizontal co-seismic displacements in the
vicinity of the fault. Pre-earthquake photographs were acquired during the summer 1989 while
post-earthquake were acquired during the autumn 1995. The footprint of each pair is slightly less
than $10 \times 10 \text{ km}^2$ and the dataset covers almost the entire surface rupture of the fault (Figs 2 and
7(a)). Because of their near-field coverage, optical data can finely constrain shallow slip in our

1 6 *B. Gombert*
2
3
4
5
6
7
8
9
10
11
12
13
14
15
16
17
18
19
20
21
22
23
24
25
26
27
28
29
30
31
32
33
34
35
36
37
38
39
40
41
42
43
44
45
46
47
48
49
50
51
52
53
54
55
56
57
58
59
60

models. However, as pointed out by Kaneko & Fialko (2011), near-fault observations may include inelastic effects that can bias slip estimates assuming linear elasticity. To avoid such artifact, we remove any near-fault pixels within 300 m of the fault. This cut-off length is in agreement with measurements by Milliner et al. (2015) showing that off-fault deformation is generally limited to a narrow zone around the fault (with an average half-width smaller than 80 m). Removing data in the vicinity of the fault also reduces the impact of modeling errors due to fault parameterization. Indeed, the assumption of constant slip in fault patches and the discretization of the fault trace (every \sim 1.5 km) induce artifacts in the predicted deformation field very close to the fault (See supporting information T1 and Fig. S2). In addition, using the same technique as for InSAR data in section 2.2, each image is downsampled and data covariance is estimated using empirical co-variograms. The resulting standard deviation is typically around 30 cm and the correlation length ranges from 300 m to 1 km. Most of the post-seismic deformation is included in the timespan separating the two acquisitions (Fialko 2004a). However, as mentioned by Milliner et al. (2015), the detection threshold of optical image correlation is about 10 cm, suggesting that \sim 15 cm of near-field post-seismic deformation lie in the uncertainties of the measurement.

110 3 PROBABILISTIC SLIP INVERSION

111 3.1 Model parametrization

112 While most previous studies used relatively simplified linear geometries, our fault parametrization
113 shown in Fig. 3 consists of nine segments following the surface rupture trace. The three main
114 segments are the Johnson Valley, Homestead Valley, and Emerson and Camp Rock faults (Sieh
115 et al. 1993). Those three segments are linked by two small junctions and completed by the small

A Bayesian exploration of the Landers Earthquake 7

1 Galway Lake Fault in the northern part of the rupture. In addition, we parametrize two antithetic
2 faults on the eastern side of the Emerson segment. These two faults were not directly mapped by
3 Sieh et al. (1993) but have been previously incorporated as linear segments by Fialko (2004b) from
4 the distribution of aftershocks. In the present study, the northern antithetic segment is refined as
5 a curved fault from the detailed analysis of InSAR ground deformation profiles along with the
6 Hauksson et al. (2012) relocated earthquake catalog (see Fig. 3). Finally, we use an additional
7 fault corresponding to the $M_w = 6.5$ Big Bear aftershock, which orientation is derived from the
8 Hauksson et al. (2012) catalog. Consistent with Fialko (2004b), faults segments are assumed to
9 be vertical and to extend down to 15 km. Although this depth is roughly in agreement with the
10 maximum depth of aftershock, we cannot exclude a more complex geometry at depth as often
11 reported when multiple fault segments interact (Segall & Pollard 1980). To evaluate the effect of
12 such complexities, we propose an alternative geometry in which shallow parallel branches merge
13 on a single deeper segment. This geometry is similar to a flower structure that can be observed in
14 some strike-slip faults (e.g., Zigone et al. 2015).

15 For both assumed fault geometries, each segment is discretized in four rows of subfaults ex-
16 tending down to 1.5 km, 4.5 km, 9.0 km, and 15.0 km depth. The size of each subfault is designed
17 to have an acceptable resolution at depth (resolution $R \geq 0.8$ as defined in the Supplementary
18 Material for the strike-slip component, see Fig. S3). This strategy ensures small posterior model
19 uncertainty but more importantly, it enables good convergence of the Bayesian sampling algorithm
20 used for the inversion.

1 8 *B. Gombert*
2
3
4

5
6 **3.2 Bayesian sampling**
7
8
9

10
11 We use a Bayesian approach to obtain the full posterior probability density function (PDF) of the
12 slip distribution given the observations and uncertainties. According to the Bayes-Laplace theorem,
13 we write the posterior PDF as:
14
15

$$p(\mathbf{m}|\mathbf{d}_{\text{obs}}) \propto p(\mathbf{m}) \exp \left[-\frac{1}{2} (\mathbf{d}_{\text{obs}} - \mathbf{G}\mathbf{m})^T \mathbf{C}_\chi^{-1} (\mathbf{d}_{\text{obs}} - \mathbf{G}\mathbf{m}) \right] \quad (1)$$

16
17 where \mathbf{m} is the model vector, $p(\mathbf{m})$ is the prior distribution, \mathbf{d}_{obs} is the data vector, \mathbf{G} is the Green
18 functions matrix, and \mathbf{C}_χ is the misfit covariance describing both data and forward prediction
19
20 uncertainties. We compute the Greens functions for a semi-infinite stratified elastic medium using
21
22 the EDKS software (Zhu & Rivera 2002)
23
24
25

26 To sample the model space we use AlTar, a parallel Markov Chain Monte Carlo (MCMC)
27 algorithm based on the CATMIP formalism (Minson et al. 2013). Using multiple MCMC chains
28 in parallel, AlTar initially samples the prior PDF, $p(\mathbf{m})$, and then slowly increases the information
29 brought by the data until it samples the posterior PDF. The implementation benefits from the use
30 of high efficiency Graphic Processing Units (GPUs), allowing us to run more than 500 000 chains
31
32 in parallel. Our final solution consists of an ensemble of models that are statistically distributed
33 according to the posterior PDF. No spatial smoothing constraint is used in this procedure. We
34
35 adopt different priors for the two different slip directions. The strike-slip component prior is a
36 uniform PDF between -1 m and 30 m, hence promoting right-lateral faulting. The dip-slip prior is
37
38 a Gaussian PDF centered on 0 m with a standard deviation of 5 m.
39
40
41
42
43
44
45
46
47
48
49
50
51
52
53
54
55
56
57
58
59
60

3.3 Model prediction uncertainties

Accounting for uncertainties in our forward predictions uncertainties is crucial since they corresponds to one of the largest sources of variability between published slip models. Moreover, these uncertainties are important in our Bayesian framework as we do not use smoothing regularization. The model prediction uncertainties are described by the matrix \mathbf{C}_p , which is added to the observation uncertainties matrix \mathbf{C}_d to obtain the misfit covariance:

$$\mathbf{C}_x = \mathbf{C}_d + \mathbf{C}_p \quad (2)$$

We build \mathbf{C}_p using the approach of Duputel et al. (2014) to account for uncertainties in the elastic model used to compute the Green's functions. The layered elastic model used in this study is derived from the Southern California Earthquake Center 3D velocity model (Kohler et al. 2003). Uncertainties on the elastic parameters are inferred by comparing different models in the source region (Fig. S4).

3.4 Probabilistic slip model

Using our Bayesian framework, we generate 500 000 models representing our posterior information on slip distribution given available geodetic data. To interpret this ensemble, we need to extract a representative model and the corresponding uncertainties. In Fig. 4, we show the posterior mean model (i.e., the average of all sampled models) along with 95% confidence ellipses. A more detailed view is available in Fig. S5. The posterior mean model is a common choice as the Bayesian approach encourages one to think in terms of an ensemble solution instead of one single model. However, as shown in Fig. S6, other models can also be depicted such as the posterior mode model (i.e., using maximum value of each marginal PDF) or the best fitting model (i.e., providing a maxi-

1 10 *B. Gombert*

2
3 166 mum posterior value). In our case, the latter models are actually very similar to the posterior mean
4
5 167 model since most marginal PDFs are nearly symmetric.

6
7 168 The results in Fig. 4 are based on vertical fault segments. They can be compared with the
8
9 169 solution in Fig. S7 obtained assuming a more complicated flower parameterization introduced in
10
11 170 section 3.1. The inferred slip distribution are fairly similar in both geometries, showing the lack of
12
13 171 sensitivity to the parametrization at depth. Thus, in the following, we focus on the results obtained
14
15 172 using vertical fault segments.

16
17 173 As expected, we observe predominately strike-slip motion along the entire fault system. Most
18
19 174 of the slip concentrates along the central and northern parts of the rupture, with a peak amplitude of
20
21
22 175 ~ 11 m. These features are to first order comparable to previous results, although published models
23
24 176 have lower peak slip amplitudes (Cohee & Beroza 1994, Fialko 2004*b*, Xu et al. 2016, e.g.). This
25
26 177 difference is probably due to smoothing imposed in previous studies that decreases the maximum
27
28 178 slip amplitude. The two small junctions (shown in Fig. S5) show relatively large slip at depth,
29
30 179 although they are associated with significant posterior uncertainties. In addition, these estimates
31
32 180 are associated with significant along-dip correlation of slip amplitudes (cf., Fig. S8).

33
34 181 The model predictions reproduce the observations reasonably well. The performance of the
35
36 182 models for GPS and trilateration data is presented in Fig. 5 with associated posterior uncertainties.
37
38 183 Posterior mean InSAR predictions and residuals are shown in Fig. 6. We observe some moderate
39
40 184 residuals in the vicinity of the fault, mainly due to the finiteness of the fault patches. Some larger
41
42 185 wavelength residuals are visible on the southern part of the descending track. We suspect that this
43
44 186 signal originates from post-seismic deformation (Fialko 2004*a*) as the second pass of this track is

1
2
3 187 5 weeks after the mainshock. Finally, our model explains reasonably well the optical correlation
4
5 188 images despite large uncertainties associated with this dataset (Fig. 7).
6
7
8
9

10 189 **3.5 Model prediction for long period seismological data**
11
12

13 190 We compute moment tensors and centroid locations equivalent to our posterior ensemble of slip
14
15 191 models. The resulting solution presented in Fig. 8 has a scalar moment $M_0 = 9.15 \pm 0.38 \times 10^{19}$
16
17 192 N.m corresponding to a moment magnitude $M_w = 7.2$.
18
19

20 193 Using this equivalent moment tensor source, we then compute waveform predictions for vari-
21
22 194 ous broadband seismological stations. We assume a triangular source time function following the
23
24 195 Global CMT (Ekström et al. 2012) parameters (a 19.2 s half-duration and 17.7 s centroid time-
25
26 196 shift). Synthetics are computed by simulating the wavefield in the 3D Earth model S362ANI (Kus-
27
28 197 towski et al. 2008) using SPECFEM3D_GLOBE (Komatitsch & Tromp 2002). We then compare
29
30 198 the observed and predicted waveforms after bandpass filtering in the 100–500 s period range using
31
32 199 a 4th-order butterworth causal filter. As shown in Figs 8, S9 and S10, the predictions agree remark-
33
34 200 ably well with the observed waveforms. This result shows that our solution is consistent with long
35
36 201 period seismological observations both in terms of seismic moment and source mechanism.
37
38
39
40
41

42 202 **3.6 Shallow slip deficit**
43
44

45 203 A shallow slip deficit is commonly observed for large strike-slip earthquakes (Simons et al. 2002,
46
47 204 Fialko et al. 2005). Although, in a simple linear elastic model, a uniform slip distribution at depth
48
49 205 is expected when averaged over many seismic cycles (Tse & Rice 1986), this deficit does not
50
51 206 seem to be recovered by either inter-seismic creep or post-seismic deformation (Fialko 2004a).
52
53
54
55
56
57
58
59
60

12 *B. Gombert*

²⁰⁷ Some exceptions have nonetheless been documented such as the 2013 $M_w = 7.7$ Balochistan
²⁰⁸ earthquakes (Jolivet et al. 2014, Vallage et al. 2015).

Although a shallow slip deficit is observed in most published models of the Landers earthquake, there is a large variability in the actual amount of shallow slip deficit between different inversion results. To investigate this, we compute the normalized potency as a function of depth:

$$P_k = \frac{\sum_i \Delta u_{ik} \times A_{ik}}{w_k} \quad (3)$$

where Δu_{ik} is the slip inferred in a patch of area A_{ik} and width w_k located in the k -th row and at an along-strike position i . This formulation allows us to avoid any bias due to the increase of patch size with depth. As shown in Fig. 4, we find a maximum potency on the 3rd row of patches (i.e., between 4.5 and 9 km depth, consistent with Simons et al. (2002)) that is nearly 1.7 times larger than surface estimates (i.e., at depth between 0 and 1.5 km). To highlight this for individual fault segments, we define the percentage of shallow slip deficit (SSD) as:

$$SSD = 100 \left(\frac{P_{k=3} - P_{k=1}}{P_{k=3}} \right) \quad (4)$$

According to this definition, $SSD > 0$ indicates some amount of shallow slip deficit while $SSD \leq 0$ means that potency is equal or larger at the surface than at depth (i.e., no shallow slip deficit). The posterior distribution of SSD is shown in Fig. 4 for the three main fault segments and the overall rupture. Results and probability estimates are also summarized in Table 1.

Although the overall rupture depicts a shallow slip deficit of about 41%, we find different behaviors for different fault segments. We observe the smallest deficit along the Emerson and Camp Rock segment where the probability of shallow slip deficit is only 0.62. The Johnson Valley fault is more likely to present a shallow deficit, but the SSD is relatively moderate ($SSD \sim 25\%$).

A Bayesian exploration of the Landers Earthquake 13

1
2
3 217 The largest deficit is measured for the Homestead Valley fault where the mean SSD is 52% with a
4
5 218 probability close to 1 that the deficit is larger than 25%. The remaining fault segments are either too
6
7 219 small, with too large uncertainties or did not slip enough to contribute significantly to the overall
8
9 220 rupture estimate. As shown in Fig. 4, these estimates somewhat agree with the model of Fialko
10
11 221 (2004b) but are generally larger than results of Cotton & Campillo (1995).
12
13
14
15
16
17
18 222 **4 DISCUSSION**
19
20
21 223 Among the different artifacts affecting co-seismic slip models, inelastic strain in the vicinity of the
22
23 224 fault is often suggested to explain the inferred shallow slip deficit (e.g., Simons et al. 2002, Fialko
24
25 225 et al. 2005). Such inelastic response can indeed bias slip inversions that are based on elastic Green's
26
27 226 functions and artificially decrease the amount of slip at shallow depth (Kaneko & Fialko 2011).
28
29
30 227 However, as reported by Milliner et al. (2015), inelastic strain for the 1992 Landers earthquake
31
32 228 is limited to a relatively narrow region around the fault (e.g., within ~65 m of the fault trace in
33
34 229 Fig. 9c). To avoid any strong bias due to our elastic assumption and reduce modeling errors due
35
36 230 to fault discretization at shallow depth, we have removed displacement data within a minimum
37
38 231 distance of 300 m from the fault trace (see section 2.3). This procedure is roughly equivalent to
39
40 232 localizing the inelastic contribution of the strain field onto an idealized fault plane (Dahlen &
41
42 233 Tromp 1998). Although removing near-fault pixels should reduce artifacts due to inelastic effects,
43
44 234 unaccounted lateral heterogeneities due to accumulated damage around the fault can also have a
45
46 235 significant impact on surface deformation patterns and by extension on the inverted slip distribution
47
48 236 (Barbot et al. 2008).
49
50
51
52
53
54
55
56 237 The fault zone is often regarded as a highly deformed core surrounded by a more or less broad
57
58
59
60

1 14 *B. Gombert*
2
3
4
5
6
7
8
9
10
11
12
13
14
15
16
17
18
19
20
21
22
23
24
25
26
27
28
29
30
31
32
33
34
35
36
37
38
39
40
41
42
43
44
45
46
47
48
49
50
51
52
53
54
55
56
57
58
59
60

238 damage zone of reduced stiffness (e.g. Chester et al. 1993, Ben-zion & Sammis 2003, Mitchell &
239 Faulkner 2009, Dor et al. 2006). The damage zone consists of cracks and microfractures in the host
240 rock and can be associated with secondary faults reducing the elastic strain released on the main
241 rupture interface (Chester & Chester 1998, Dieterich & Smith 2009). Such secondary dislocations
242 have been reported around the Landers fault system (McGill & Rubin 1999). An example is given
243 in Fig. 9, showing two secondary ruptures (labeled F1 and F2) visible in optical correlation images
244 near the Emerson Valley fault. Such off-fault dislocations are not accounted for in our slip model
245 presented in Fig. 4.

246 To investigate the properties of the damage zone and secondary ruptures, we analyze a profile
247 across the fault using simple vertical elastic screw dislocations embedded in a compliant fault zone
248 (Segall 2010). Using a Metropolis algorithm, we invert for the slip distribution on each fault, a
249 compliant zone half-width and an effective shear modulus contrast μ_1/μ_0 (where μ_1 is the shear
250 modulus of the fault zone while μ_0 is the modulus of the surrounding crust). The compliant zone
251 half-width and shear modulus ratio being typical Jeffreys parameters (Tarantola 2005), they are
252 sampled in log domain. To avoid any effect of off-fault inelasticity, we remove the data within
253 65 m of the fault, which is consistent with fault-width measurements by Milliner et al. (2015)
254 at this location. The results presented in Fig. 9(c) indicate very shallow secondary ruptures with
255 32 ± 8 cm and 36 ± 5 cm of slip down to 84 ± 30 m and 180 ± 40 m respectively for faults F1 and F2.
256 Although such slip amplitudes are not negligible, these off-fault dislocations are relatively shallow
257 and thus represent only 3.3% of the total seismic slip inferred from the surface down to 0.5 km. Of
258 course, these measurements are only valid locally since the properties of secondary faults might

A Bayesian exploration of the Landers Earthquake 15

1
2
3 vary significantly along the main rupture (Lewis & Ben-Zion 2010, Milliner et al. 2015, Thomas
4
5 et al. 2017).
6
7

8 The results shown in Fig. 10 highlight the existence of a \sim 1.1 km wide compliant zone around
9 this part of the fault. Although there is some correlation between the compliant zone width and
10
11 rigidity, our solution indicates that shear modulus can be reduced by as much as a factor \sim 5 within
12
13 the damage zone (i.e., a shear modulus ratio of \sim 0.2). This estimate is consistent with measure-
14
15 ments from guided seismic waves (Li et al. 2007, 1994, Peng et al. 2003) that indicate shear mod-
16
17 ulus ratios between 0.1 and 0.4, corresponding to 80% of our models. On the other hand, these
18
19 studies suggest relatively small damage zone widths of a few hundred meters, which is narrower
20
21 than our estimates.
22
23
24

25 Using the aftershock catalog of Hauksson et al. (2012), we compare our estimates with the
26 distribution of seismicity around the main fault, which is another indicator of distributed damage
27 in the host rock (Amitrano 2006, Powers & Jordan 2010). As shown in Fig. 11(a), we select two
28 profiles across the main rupture surrounding the southern antithetic fault to avoid any bias due to
29 events located on this segment. Following Powers & Jordan (2010), we compute the horizontal
30 density $\nu(x)$ of seismicity where x is the fault normal distance, and assume a power law decay of
31
32 the form
33
34

$$\nu(x) = \nu_0 \left(1 + \frac{x^2}{d^2}\right)^{-\gamma/2} \quad (5)$$

35
36
37
38
39
40
41
42
43
44
45
46
47
48
49 where ν_0 is the aftershock density at $x = 0$, d is the damage zone half-width and γ is the asymptotic
50
51 roll-off of the seismicity away from the fault. Using a Metropolis inversion scheme, we then sample
52
53
54
55
56
57
58
59
60 ν_0 , d , and γ given the seismicity density, $\nu(x)$. Comparison between observations and stochastic
predictions are shown in Fig. 11(b) and the full posterior PDFs for the 3 parameters are shown in

1 16 *B. Gombert*

2
3 Fig. S11. Although the posterior mean damage-zone half-width $d \sim 800$ m is larger than what is
4 inferred from optical images ($d \sim 570$ m), an inversion with a fixed $d = 570$ m also explains the
5 data reasonably well (cf. Fig. 11(b)).
6
7
8
9

10 To estimate the impact of the damage zone on the inverted slip distribution, we also invert
11 the fault-parallel displacement profile of Fig. 9(c) without a compliant zone and after removing the
12 data within 300 m of the fault (i.e. the same way it is done in our main slip inversion). The posterior
13 PDFs of shallow slip and stochastic predictions with and without accounting for the damage zone
14 are shown in Fig. 12. Although far field deformation is well-predicted in both inversions, predic-
15 tions neglecting a compliant zone fail to reproduce near-fault observations and underestimate slip
16 at shallow depth. On average, accounting for the compliant zone increases shallow slip by a factor
17 of 1.2. On the other hand, neglecting lateral shear modulus heterogeneities will systematically lead
18 to smaller slip (with a probability of 98%). To roughly estimate the effect of the damage zone,
19 we can empirically correct the surface mean slip of the Landers rupture by factors drawn from
20 posterior PDFs with and without accounting for the compliant zone. Results presented in Fig. 13
21 and Table 1, indicate that this significantly reduces the overall shallow slip deficit from 41% to
22 27%. These results should, however, be considered with caution, as the damage behavior can vary
23 significantly along the fault (Lewis & Ben-Zion 2010). We tried to conduct similar experiments in
24 other locations on the fault but did not obtain reliable constraints on the compliant zone param-
25 eters (see for example Figs S12 and S13). Even if damage properties can widely vary along the
26 fault, such structures will necessarily impact slip estimated at shallow depth, thereby reducing the
27 inferred shallow deficit.
28
29
30
31
32
33
34
35
36
37
38
39
40
41
42
43
44
45
46
47
48
49
50
51
52
53
54
55
56
57
58
59
60

5 CONCLUSION

We used an extensive geodetic dataset, careful uncertainty estimates and a realistic fault geometry to produce a stochastic finite-fault model of the Landers earthquake. Our Bayesian approach to the inversion has two main advantages: (1) the solution is not biased by any kind of smoothing and (2) posterior parameter uncertainties are available and provide valuable information on the validity of the model. The predictions from our solution agree well with various observations. This solution is also consistent with long period data seismological data that are well predicted by waveform synthetics computed from our model.

Consistent with previous studies, our solution indicates a substantial shallow slip deficit that is particularly pronounced for the Homestead Valley Fault. We argue that part of this deficit results from unmodeled lateral heterogeneities in shear modulus, corresponding to a damage zone surrounding the fault. Using high resolution optical correlation images, we highlight a ~ 1 km wide damage zone on the Emerson Valley Fault responsible for an apparent reduction in shallow slip by a factor ~ 1.2 . Our results also show the presence of secondary ruptures with significant slip amplitudes at shallow depth. By reducing the elastic strain on the main fault, these features also contribute to the apparent slip deficit budget.

Although we do not include data in the immediate vicinity of the fault where inelastic behavior is commonly observed, we cannot rule out that some wide plastic deformation is included in our inversion and participates in the observed deficit. Following the same procedure, other near-field displacement data of large strike-slip earthquakes could provide new insights on fault zone properties and their link to co-seismic slip distribution.

1 18 *B. Gombert*
2
3
4
5

6 315 **6 ACKNOWLEDGMENT**
7
8
9
10
11
12
13
14
15
16
17
18
19
20
21
22
23
24
25
26
27
28
29
30
31
32
33
34
35
36
37
38
39
40
41
42
43
44
45
46
47
48
49
50
51
52
53
54
55
56
57
58
59
60

316 We are grateful to J.P. Avouac and F. Ayoub for providing the optical images correlation obser-
317 vations. We also thank Y. Fialko for sending us his co-seismic slip model. This study contributed
318 from fruitful discussions with Sarah Minson, Lijun Zhu, Michael Aivazis and Gilles Peltzer. Some
319 GPUs used for this research were donated by the NVIDIA Corporation. This work was supported
320 by the Initiative d'Excellence (IDEX) funding framework (Universit de Strasbourg) and the CNRS
321 PICS program (Zacharie Duputel). This work was also funded by NSF grant 1447107 awarded to
322 Mark Simons.

323 **References**

- 324 Aki, K. & Richards, P. G. (2009), *Quantitative seismology*, 2. ed., print edn, Univ. Science Books.
- 325 Amitrano, D. (2006), 'Rupture by damage accumulation in rocks', *International Journal of Frac-*
ture **139**(34), 369381.
- 326 Ayoub, F., Leprince, S. & Avouac, J.-P. (2009), 'Co-registration and correlation of aerial pho-
- 327 tographs for ground deformation measurements', *ISPRS Journal of Photogrammetry and Re-*
mote Sensing **64**(6), 551–560.
- 328 Backus, G. & Mulcahy, M. (1976), 'Moment tensors and other phenomenological descriptions
- 329 of seismic sources i. continuous displacements', *Geophysical Journal of the Royal Astronomical*
Society **46**(2), 341361.
- 330 Barbot, S., Fialko, Y. & Sandwell, D. (2008), 'Effect of a compliant fault zone on the inferred
- 331 earthquake slip distribution', *Journal of Geophysical Research* **113**(B6).
- 332 Ben-Zion, Y. & Ampuero, J.-P. (2009), 'Seismic radiation from regions sustaining material dam-
- 333 age', *Geophysical Journal International* **178**(3), 13511356.
- 334 Ben-zion, Y. & Sammis, C. G. (2003), *Characterization of Fault Zones*, Pageoph Topical Vol-
- 335 umes, Birkhäuser Basel, p. 677715.
- 336 Chen, Q. & Freymueller, J. T. (2002), 'Geodetic evidence for a near-fault compliant zone along
- 337 the san andreas fault in the san francisco bay area', *Bulletin of the Seismological Society of*
America **92**(2), 656671.
- 338 Chester, F., Chester, J., Kirschner, D., Schulz, S. & Evans, J. (2004), 'Structure of large-
- 339 displacement, strike-slip fault zones in the brittle continental crust', *Rheology and Deformation*
in the Lithosphere at Continental Margins **1**, 223–260.

1 20 *B. Gombert*

2
3 345 Chester, F. M. & Chester, J. S. (1998), 'Ultracataclasite structure and friction processes of the
4
5 346 punchbowl fault, san andreas system, california', *Tectonophysics* **295**(12), 199221.

6
7 347 Chester, F. M. & Chester, J. S. (2000), 'Stress and deformation along wavy frictional faults',
8
9 348 *Journal of Geophysical Research: Solid Earth* **105**(B10), 2342123430.

10
11 349 Chester, F. M., Evans, J. P. & Biegel, R. L. (1993), 'Internal structure and weakening mechanisms
12
13 350 of the san andreas fault', *Journal of Geophysical Research: Solid Earth* **98**(B1), 771786.

14
15 351 Cohee, B. P. & Beroza, G. C. (1994), 'Slip distribution of the 1992 Landers earthquake and its
16
17 352 implications for earthquake source mechanics', *Bulletin of the Seismological Society of America*
18
19 353 **84**(3), 692–712.

20
21 354 Cotton, F. & Campillo, M. (1995), 'Frequency domain inversion of strong motions: Application
22
23 355 to the 1992 landers earthquake', *Journal of Geophysical Research* **100**(B3), 3961.

24
25 356 Dahlen, F. A. & Tromp, J. (1998), *Theoretical global seismology*, Princeton University Press.

26
27 357 Dieterich, J. H. & Smith, D. E. (2009), 'Nonplanar faults: Mechanics of slip and off-fault dam-
28
29 358 age', *Pure and Applied Geophysics* **166**(1011), 17991815.

30
31 359 Dokka, R. K. & Travis, C. J. (1990), 'Role of the eastern california shear zone in accommodating
32
33 360 pacific-north american plate motion', *Geophysical Research Letters* **17**(9), 13231326.

34
35 361 Dor, O., Ben-Zion, Y., Rockwell, T. K. & Brune, J. (2006), 'Pulverized rocks in the mojave section
36
37 362 of the san andreas fault zone', *Earth and Planetary Science Letters* **245**(34), 642654.

38
39 363 Duputel, Z., Agram, P. S., Simons, M., Minson, S. E. & Beck, J. L. (2014), 'Accounting for
40
41 364 prediction uncertainty when inferring subsurface fault slip', *Geophysical Journal International*
42
43 365 **197**(1), 464482.

44
45 366 Ekström, G., Nettles, M. & Dziewonski, A. (2012), 'The global cmt project 20042010:

46
47
48
49
50
51
52
53
54
55
56
57
58
59
60

A Bayesian exploration of the Landers Earthquake 21

- 1
2
3 367 Centroid-moment tensors for 13,017 earthquakes', *Physics of the Earth and Planetary Interi-*
4
5 368 *ors* **200201**, 19.
6
7
8 369 Fialko, Y. (2004a), 'Evidence of fluid-filled upper crust from observations of postseismic defor-
9
10 370 mation due to the 1992 mw7.3 landers earthquake', *Journal of Geophysical Research: Solid*
11
12 371 *Earth* **109**(B8), B08401.
13
14
15 372 Fialko, Y. (2004b), 'Probing the mechanical properties of seismically active crust with space
16
17 373 geodesy: Study of the coseismic deformation due to the 1992 M_w 7.3 Landers (southern Cali-
18
19 374 fornia) earthquake', *Journal of Geophysical Research* **109**(B3).
20
21
22 375 Fialko, Y., Sandwell, D., Agnew, D., Simons, M., Shearer, P. & Minster, B. (2002), 'Deformation
23
24 376 on nearby faults induced by the 1999 hector mine earthquake', *Science* **297**(5588), 18581862.
25
26
27 377 Fialko, Y., Sandwell, D., Simons, M. & Rosen, P. (2005), 'Three-dimensional deformation caused
28
29 378 by the Bam, Iran, earthquake and the origin of shallow slip deficit', *Nature* **435**(7040), 295–299.
30
31
32 379 Freymueller, J., King, N. E. & Segall, P. (1994), 'The co-seismic slip distribution of the Landers
33
34 380 earthquake', *Bulletin of the Seismological Society of America* **84**(3), 646–659.
35
36
37 381 Hansen, P. C. (1998), *Rank-Deficient and Discrete Ill-Posed Problems: Numerical Aspects of*
38
39 382 *Linear Inversion*, Society for Industrial and Applied Mathematics.
40
41
42 383 Hartzell, S. H. & Heaton, T. H. (1983), 'Inversion of strong ground motion and teleseismic wave-
43
44 384 form data for the fault rupture history of the 1979 imperial valley, California, earthquake', *Bul-*
45
46 385 *letin of the Seismological Society of America* **73**(6A), 15531583.
47
48
49 386 Hauksson, E., Yang, W. & Shearer, P. M. (2012), 'Waveform relocated earthquake catalog for
50
51 387 southern California (1981 to June 2011)', *Bulletin of the Seismological Society of America*
52
53 388 **102**(5), 22392244.
54
55
56
57
58
59
60

1 22 *B. Gombert*

2 389 Hudnut, K. W., Bock, Y., Cline, M., Fang, P., Feng, Y., Freymueller, J., Ge, X., Gross, W. K.,

3 390 Jackson, D., Kim, M., King, N. E., Langbein, J., Larsen, S. C., Lisowski, M., Shen, Z.-K., Svart,

4 391 J. & Zhang, J. (1994), 'Co-seismic displacements of the 1992 Landers earthquake sequence',

5 392 *Bulletin of the Seismological Society of America* **84**(3), 625–645.

6 393 Jolivet, R., Brägmann, R. & Houli, N. (2009), 'Geodetic exploration of the elastic properties

7 394 across and within the northern San Andreas fault zone', *Earth and Planetary Science Letters*8 395 **288**(12), 126131.

9 396 Jolivet, R., Duputel, Z., Riel, B., Simons, M., Rivera, L., Minson, S. E., Zhang, H., Aivazis,

10 397 M. a. G., Ayoub, F., Leprince, S. & et al. (2014), 'The 2013 mw 7.7 Balochistan earthquake:

11 398 Seismic potential of an accretionary wedge', *Bulletin of the Seismological Society of America*12 399 **104**(2), 10201030.

13 400 Kaneko, Y. & Fialko, Y. (2011), 'Shallow slip deficit due to large strike-slip earthquakes in dy-

14 401 namic rupture simulations with elasto-plastic off-fault response: Modelling shallow slip deficit',

15 402 *Geophysical Journal International* **186**(3), 13891403.

16 403 Kaneko, Y., Lapusta, N. & Ampuero, J.-P. (2008), 'Spectral element modeling of spontaneous

17 404 earthquake rupture on rate and state faults: Effect of velocity-strengthening friction at shallow

18 405 depths', *Journal of Geophysical Research* **113**(B9).

19 406 Kohler, M. D., Magistrale, H. & Clayton, R. W. (2003), 'Mantle heterogeneities and the scec

20 407 reference three-dimensional seismic velocity model version 3', *Bulletin of the Seismological*21 408 *Society of America* **93**(2), 757774.

22 409 Komatitsch, D. & Tromp, J. (2002), 'Spectral-element simulations of global seismic wave prop-

23 410 agation. validation', *Geophysical Journal International* **149**(2), 390412.

A Bayesian exploration of the Landers Earthquake 23

- 1
2
3 411 Kustowski, B., Ekström, G. & Dziewonski, A. M. (2008), 'Anisotropic shear-wave velocity struc-
4
5 412 ture of the earths mantle: A global model', *Journal of Geophysical Research: Solid Earth*
6
7 413 **113**(B6), B06306.
8
9
10
11 414 Lasserre, C., Peltzer, G., Cramp, F., Klinger, Y., Van der Woerd, J. & Tapponnier, P. (2005),
12
13 415 'Coseismic deformation of the 2001 mw = 7.8 kokoxili earthquake in tibet, measured
14
15 416 by synthetic aperture radar interferometry', *Journal of Geophysical Research: Solid Earth*
16
17 417 **110**(B12), B12408.
18
19
20
21 418 Lewis, M. A. & Ben-Zion, Y. (2010), 'Diversity of fault zone damage and trapping structures in
22
23 419 the parkfield section of the san andreas fault from comprehensive analysis of near fault seismo-
24
25 420 grams', *Geophysical Journal International* **183**(3), 15791595.
26
27
28 421 Li, H., Zhu, L. & Yang, H. (2007), 'High-resolution structures of the landers fault zone inferred
29
30 422 from aftershock waveform data: High-resolution landers fault zone structures', *Geophysical*
31
32 423 *Journal International* **171**(3), 12951307.
33
34
35
36 424 Li, Y.-G., Aki, K., Vidale, J. E., Lee, W. H. K. & Marone, C. J. (1994), 'Fine structure of the
37
38 425 landers fault zone: Segmentation and the rupture process', *Science* **265**(5170), 367370.
39
40
41 426 Lohman, R. B. & Simons, M. (2005), 'Some thoughts on the use of insar data to constrain models
42
43 427 of surface deformation: Noise structure and data downsampling', *Geochemistry, Geophysics,*
44
45 428 *Geosystems* **6**(1), Q01007.
46
47
48 429 Materna, K. & Brgmann, R. (2016), 'Contrasts in compliant fault zone properties inferred from
49
50 430 geodetic measurements in the san francisco bay area', *Journal of Geophysical Research: Solid*
51
52 431 *Earth* p. 2016JB013243.
53
54
55 432 McGill, S. F. & Rubin, C. M. (1999), 'Surficial slip distribution on the central emerson fault

1 24 *B. Gombert*2 433 during the june 28, 1992, landers earthquake, california', *Journal of Geophysical Research:*3 434 *Solid Earth* **104**(B3), 48114833.

4 435 Milliner, C. W. D., Dolan, J. F., Hollingsworth, J., Leprince, S., Ayoub, F. & Sammis, C. G.

5 436 (2015), 'Quantifying near-field and off-fault deformation patterns of the 1992 Mw 7.3 Landers

6 437 earthquake', *Geochem. Geophys. Geosyst.* **16**(5), 1577–1598.

7 438 Milliner, C. W. D., Sammis, C., Allam, A. A., Dolan, J. F., Hollingsworth, J., Leprince, S. &

8 439 Ayoub, F. (2016), 'Resolving fine-scale heterogeneity of co-seismic slip and the relation to fault

9 440 structure', *Scientific Reports* **6**, 27201.

10 441 Minson, S. E., Simons, M. & Beck, J. L. (2013), 'Bayesian inversion for finite fault earthquake

11 442 source models I—theory and algorithm', *Geophysical Journal International* **194**(3), 1701–1726.

12 443 Mitchell, T. & Faulkner, D. (2009), 'The nature and origin of off-fault damage surrounding strike-

13 444 slip fault zones with a wide range of displacements: A field study from the atacama fault system,

14 445 northern chile', *Journal of Structural Geology* **31**(8), 802816.

15 446 Murray, M. H., Savage, J. C., Lisowski, M. & Gross, W. K. (1993), 'Coseismic displacements:

16 447 1992 Landers, California, Earthquake', *Geophys. Res. Lett.* **20**(7), 623–626.

17 448 Olson, A. H. & Apsel, R. J. (1982), 'Finite faults and inverse theory with applications to the 1979

18 449 imperial valley earthquake', *Bulletin of the Seismological Society of America* **72**(6A), 19692001.

19 450 Peltzer, G., Rosen, P., Rogez, F. & Hudnut, K. (1998), 'Poroelastic rebound along the Landers

20 451 1992 earthquake surface rupture', *J. Geophys. Res.* **103**(B12), 30131–30145.

21 452 Peng, Z., Ben-Zion, Y., Michael, A. J. & Zhu, L. (2003), 'Quantitative analysis of seismic fault

22 453 zone waves in the rupture zone of the 1992 landers, california, earthquake: evidence for a shallow

23 454 trapping structure', *Geophysical Journal International* **155**(3), 10211041.

A Bayesian exploration of the Landers Earthquake 25

- 1
2
3 455 Powers, P. M. & Jordan, T. H. (2010), 'Distribution of seismicity across strike-slip faults in cali-
4
5 456 fornia', *Journal of Geophysical Research* **115**(B5).
- 6
7 457 Rosen, P. A., Hensley, S., Peltzer, G. & Simons, M. (2004), 'Updated repeat orbit interferometry
8
9 458 package released', *Eos, Transactions American Geophysical Union* **85**(5), 4747.
- 10
11 459 Roux, P., Wathélet, M. & Roueff, A. (2011), 'The san andreas fault revisited through seismic-
12
13 460 noise and surface-wave tomography', *Geophysical Research Letters* **38**(13), L13319.
- 14
15 461 Savage, J. C. & Burford, R. O. (1970), 'Accumulation of tectonic strain in california', *Bulletin of
16
17 462 the Seismological Society of America* **60**(6), 18771896.
- 18
19 463 Scholz, C. H. (1998), 'Earthquakes and friction laws', *Nature* **391**(6662), 3742.
- 20
21 464 Scholz, C. H., Dawers, N. H., Yu, J.-Z., Anders, M. H. & Cowie, P. A. (1993), 'Fault growth
22
23 465 and fault scaling laws: Preliminary results', *Journal of Geophysical Research: Solid Earth*
24
25 466 **98**(B12), 2195121961.
- 26
27 467 Segall, P. (2010), *Earthquake and volcano deformation*, Princeton University Press.
- 28
29 468 Segall, P. & Pollard, D. D. (1980), 'Mechanics of discontinuous faults', *Journal of Geophysical
30
31 469 Research: Solid Earth* **85**(B8), 43374350.
- 32
33 470 Sieh, K., Jones, L., Hauksson, E., Hudnut, K., Eberhart-Phillips, D., Heaton, T., Hough, S., Hut-
34
35 471 ton, K., Kanamori, H., Lilje, A., Lindvall, S., McGill, S. F., Mori, J., Rubin, C., Spotila, J. A.,
36
37 472 Stock, J., Thio, H. K., Treiman, J., Wernicke, B. & Zachariasen, J. (1993), 'Near-Field Investi-
38
39 473 gations of the Landers Earthquake Sequence, April to July 1992', *Science* **260**(5105), 171–176.
- 40
41 474 Simons, M., Fialko, Y. & Rivera, L. (2002), 'Coseismic deformation from the 1999 mw 7.1 hec-
42
43 475 tor mine, california, earthquake as inferred from insar and gps observations', *Bulletin of the
44
45 476 Seismological Society of America* **92**(4), 13901402.

1 26 *B. Gombert*

2
3 477 Tarantola, A. (2005), *Inverse problem theory and methods for model parameter estimation*, Soci-
4
5 ety for Industrial and Applied Mathematics.
6
7
8 478 Thomas, M. Y., Bhat, H. S. & Klinger, Y. (2017), *Effect of Brittle off-fault Damage on Earthquake*
9
10 479 *Rupture Dynamics*, AGU Geophysical Monograph Series, John Wiley & Sons.
11
12
13 480 Tse, S. T. & Rice, J. R. (1986), ‘Crustal earthquake instability in relation to the depth variation of
14
15 frictional slip properties’, *Journal of Geophysical Research* **91**(B9), 9452.
16
17
18 481 Vallage, A., Klinger, Y., Grandin, R., Bhat, H. S. & Pierrot-Deseilligny, M. (2015), ‘Inelas-
19
20 tic surface deformation during the 2013 mw 7.7 balochistan, pakistan, earthquake’, *Geology*
21
22
23 482 **43**(12), 10791082.
24
25
26 483 Vidale, J. E. & Li, Y.-G. (2003), ‘Damage to the shallow landers fault from the nearby hector
27
28 mine earthquake’, *Nature* **421**(6922), 524526.
29
30
31 484 Wald, D. J. & Heaton, T. H. (1994), ‘Spatial and temporal distribution of slip for the 1992 Landers,
32
33 California, earthquake’, *Bulletin of the Seismological Society of America* **84**(3), 668–691.
34
35
36 485 Xu, X., Tong, X., Sandwell, D. T., Milliner, C. W. D., Dolan, J. F., Hollingsworth, J., Leprince,
37
38 486 S. & Ayoub, F. (2016), ‘Refining the shallow slip deficit’, *Geophysical Journal International*
39
40
41 487 **204**(3), 18671886.
42
43
44 488 Zhu, L. & Rivera, L. A. (2002), ‘A note on the dynamic and static displacements from a point
45
46 source in multilayered media’, *Geophysical Journal International* **148**(3), 619627.
47
48
49 489 Zigone, D., Ben-Zion, Y., Campillo, M. & Roux, P. (2015), ‘Seismic tomography of the southern
50
51 490 california plate boundary region from noise-based rayleigh and love waves’, *Pure and Applied
52
53 491 Geophysics* **172**(5), 10071032.
54
55
56
57
58
59
60

498 Authors mailing address

499 Baptiste Gombert : gombert@unistra.fr
 500 Zacharie Duputel : zacharie.duputel@unistra.fr
 501 Romain Jolivet : romain.jolivet@ens.fr
 502 Cécile Doubre : cecile.doubre@unistra.fr
 503 Luis Rivera : luis.rivera@unistra.fr
 504 Mark Simons : simons@caltech.edu

505

Table 1. Shallow slip deficit estimated for different fault segments and for the whole rupture. A zero or negative SSD means that there is no deficit. A SSD value of 50% means that there is twice more slip at depth than at the surface.

Fault segment	Mean SSD	95% conf. interval	Probability than SSD is greater or equal than...		
			0%	25%	50%
Emerson and Camp Rock	2.6%	-25.1% - 33.5%	62%	3.1%	0%
Johnson Valley	25.4%	-3.8% - 57.6%	94%	58.2%	<1%
Homestead Valley	51.7%	42.7% - 61.9%	100%	97.0%	67.5%
All faults combined	40.9%	35.2% - 47.3%	100%	99.9%	<1%
All faults combined taking into account a compliant zone	29.6%	14.32% - 46.4%	99.6%	75.8%	<1%

1 28 B. Gombert
2
3
4
5
6
7
8
9
10
11
12
13
14
15
16
17
18
19
20
21
22
23
24
25
26
27
28
29
30
31
32
33
34
35
36
37
38
39
40
41
42
43
44
45
46
47
48
49
50
51
52
53
54
55
56
57
58
59
60

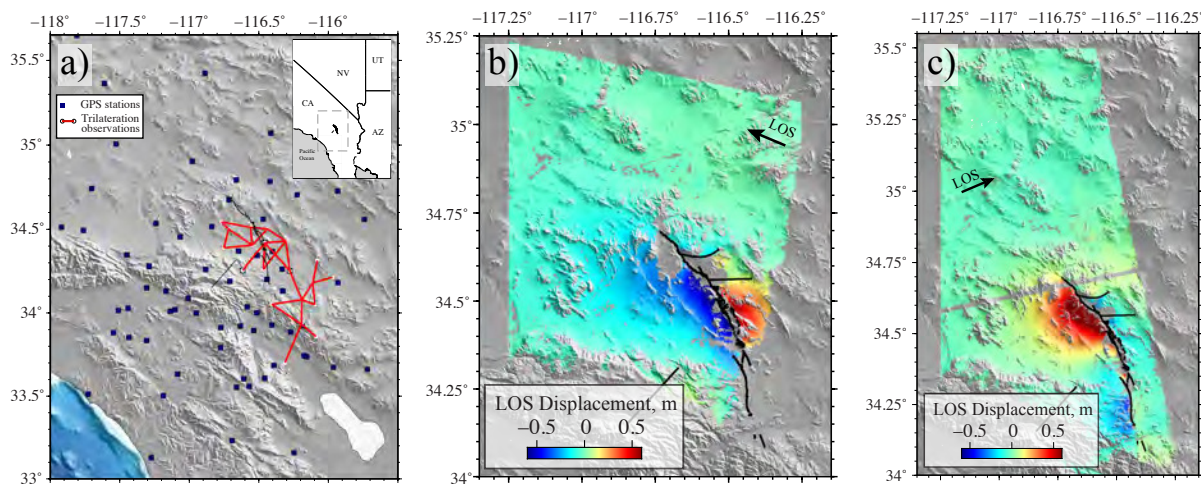


Figure 1. Far field observations used in this study. (a) General view of the study area. **(b)** InSAR observations of the ascending track. **(c)** InSAR observations of the descending track. The ascending interferogram covers the time span between 26 May to 30 June 1992 and the descending interferogram between 24 April to 7 August.

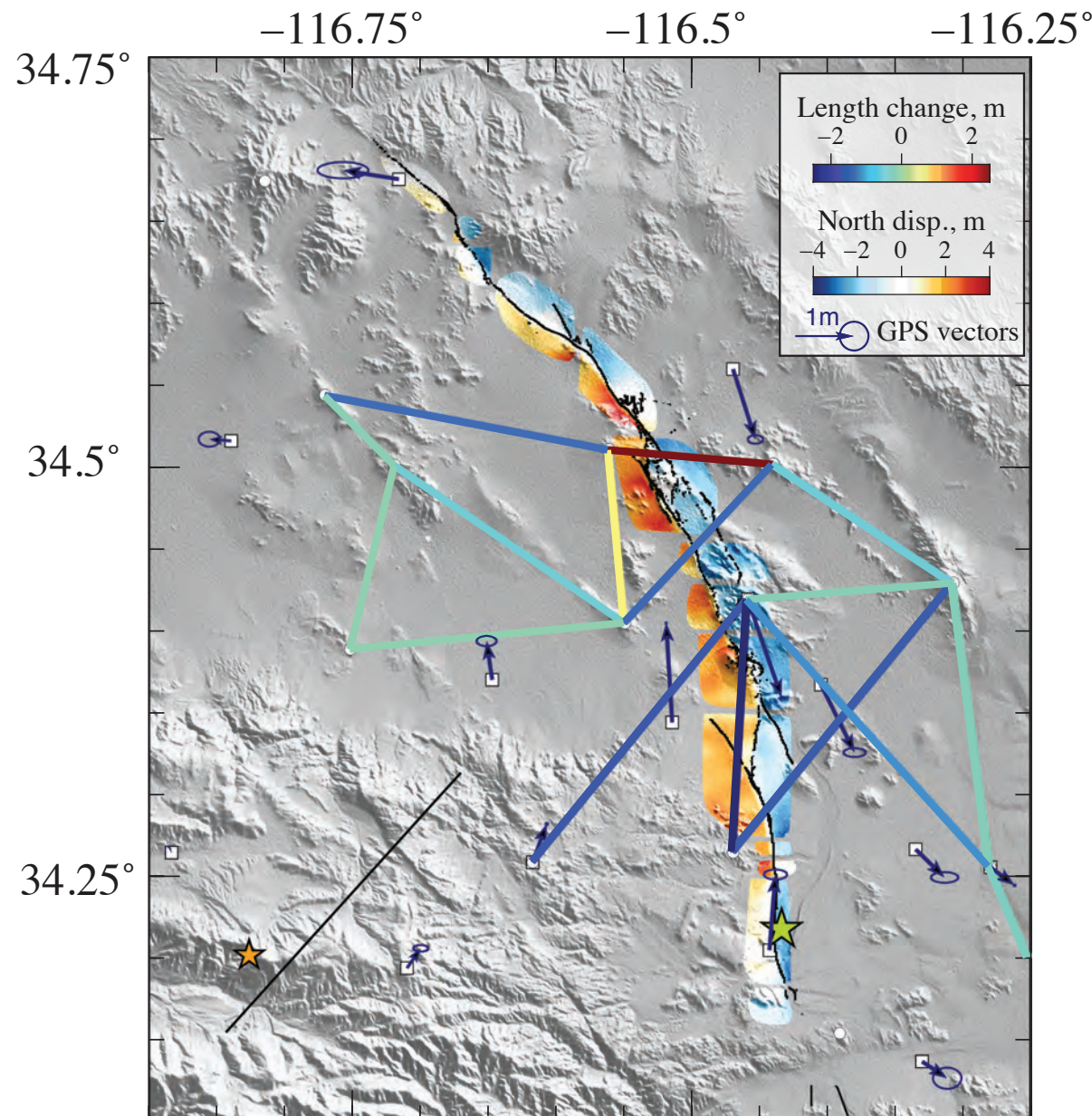


Figure 2. Near field observations. Lines are colored according to length changes in the trilateration network. The optical correlation mosaic is plotted around the fault trace from (Sieh et al. 1993). Mainshock and Big Bear aftershock ($M_w=6.5$) hypocentres from the Southern California Earthquake Center are indicated with a green and an orange star, respectively.

1
2 30 B. Gombert
3
4
5
6
7
8
9
10
11
12
13
14
15
16
17
18
19
20
21
22
23
24
25
26
27
28
29
30
31
32
33
34
35
36
37
38
39
40
41
42
43
44
45
46
47
48
49
50
51
52
53
54
55
56
57
58
59
60

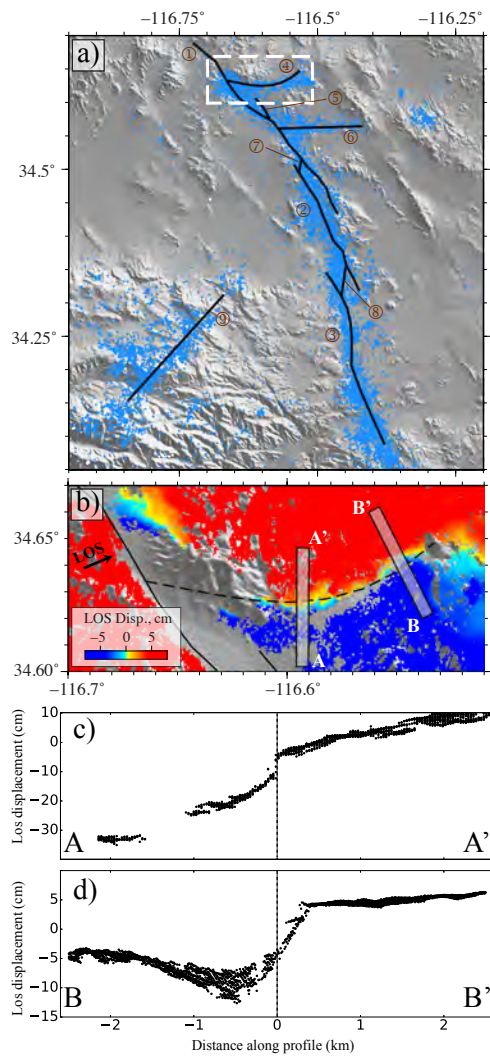


Figure 3. (a) Surface trace of the parametrized fault segments. Each segment is plotted as a thick black line. 1. Emerson and Camp Rock Faults, 2. Homestead Valley Fault, 3. Johnson Valley Fault, 4. Northern conjugate Fault, 5. Galway Lake Fault, 6. Southern conjugated Fault, 7. Emerson-Homestead Valley junction, 8. Kickapoo Fault, 9. Big Bear Fault. Blue dots represent aftershock locations from Hauksson et al. (2012). Dashed white rectangle shows the extent of (b). (b) Surface trace of the northern conjugate segment (dashed line). Rectangles show the position of the profiles shown in (c) and (d). Background color represents the InSAR ascending track LOS displacement pattern. (c) and (d) InSAR data profiles A-A' and B-B'

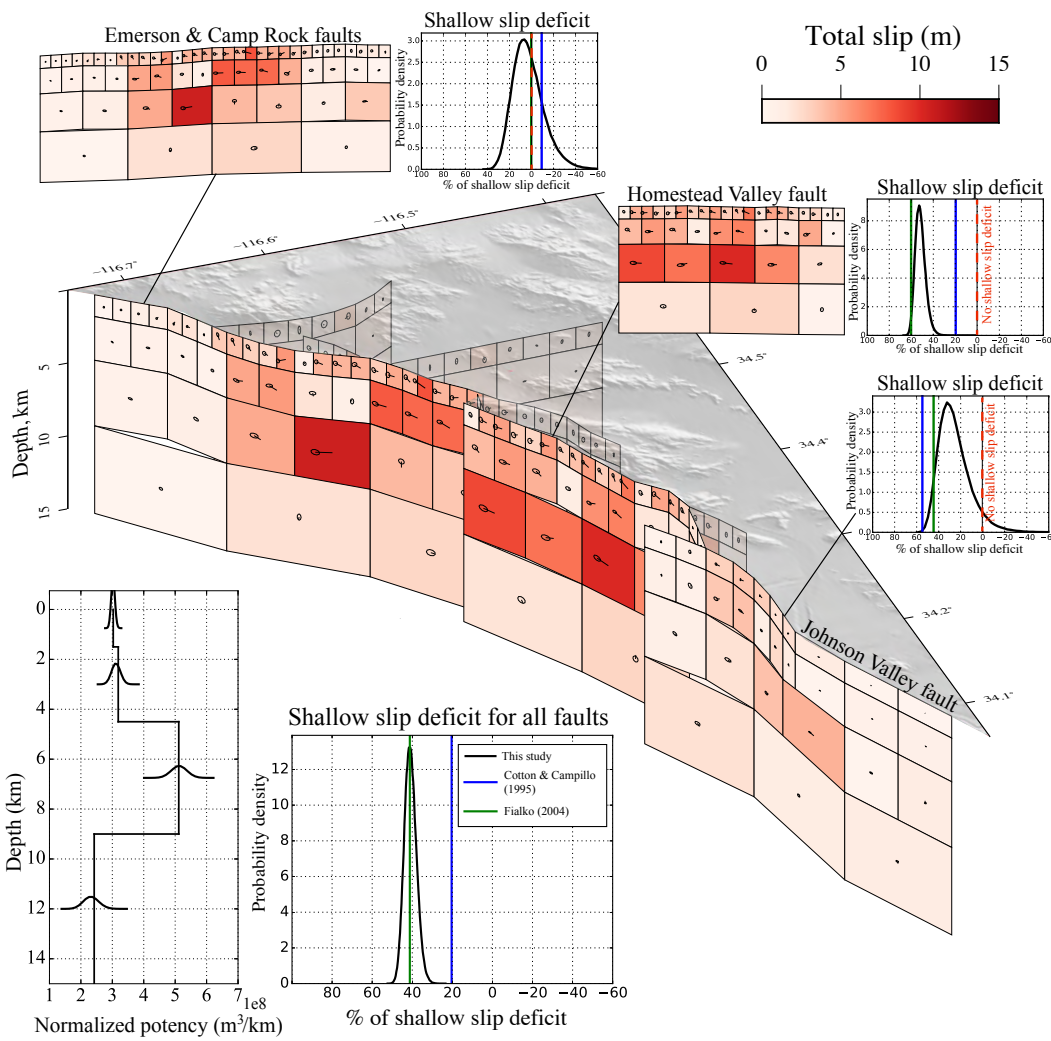


Figure 4. Posterior mean co-seismic slip model. The color of each subfault patch indicates the slip amplitude. Arrows and their associated 95% confidence ellipse indicate the slip direction and uncertainty. The bottom left inset shows the potency normalized by patch row width as a function of depth. PDFs of shallow slip deficit (SSD) are presented for the entire fault system and for individual fault segments. Vertical lines on the same plots indicate the SSD of two published models (Cotton & Campillo 1995, Fialko 2004b).

1
2 32 B. Gombert
3
4
5
6
7
8
9
10
11
12
13
14
15
16
17
18
19
20
21
22
23
24
25
26
27
28
29
30
31
32
33
34
35
36
37
38
39
40
41
42
43
44
45
46
47
48
49
50
51
52
53
54
55
56
57
58
59
60

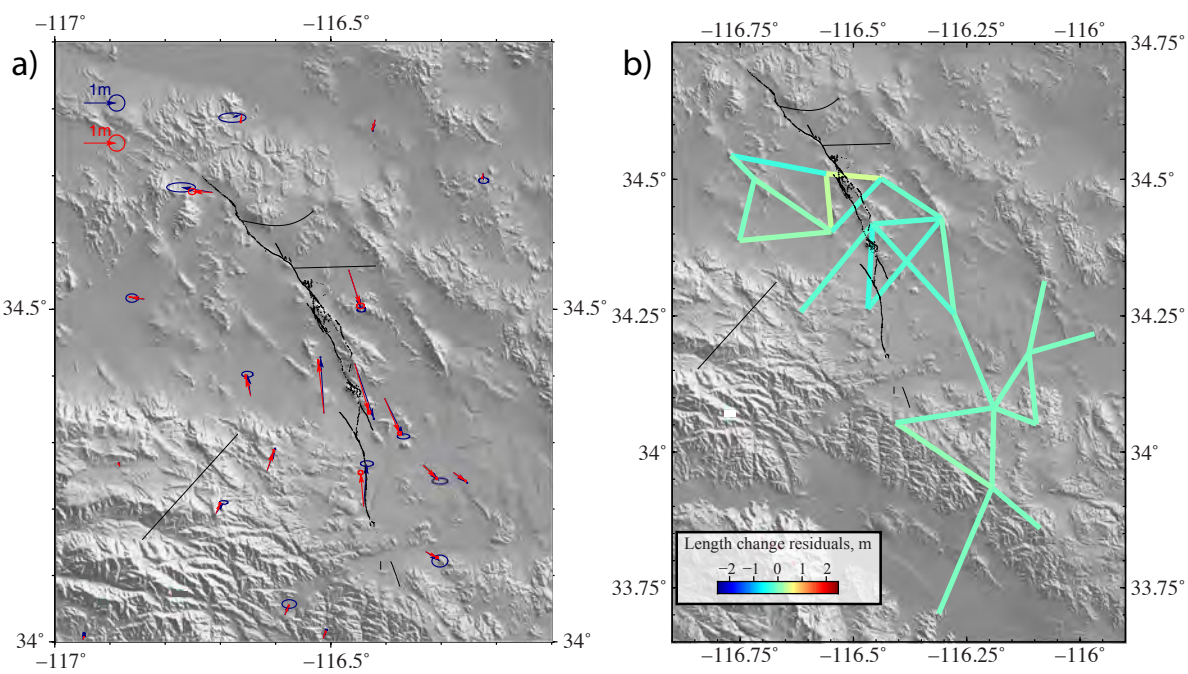


Figure 5. Model performance for GPS and trilateration data. (a) GPS observations (blue) and predictions (red) with their 1-sigma error ellipses. **(b)** Length changes residuals for the posterior mean model.

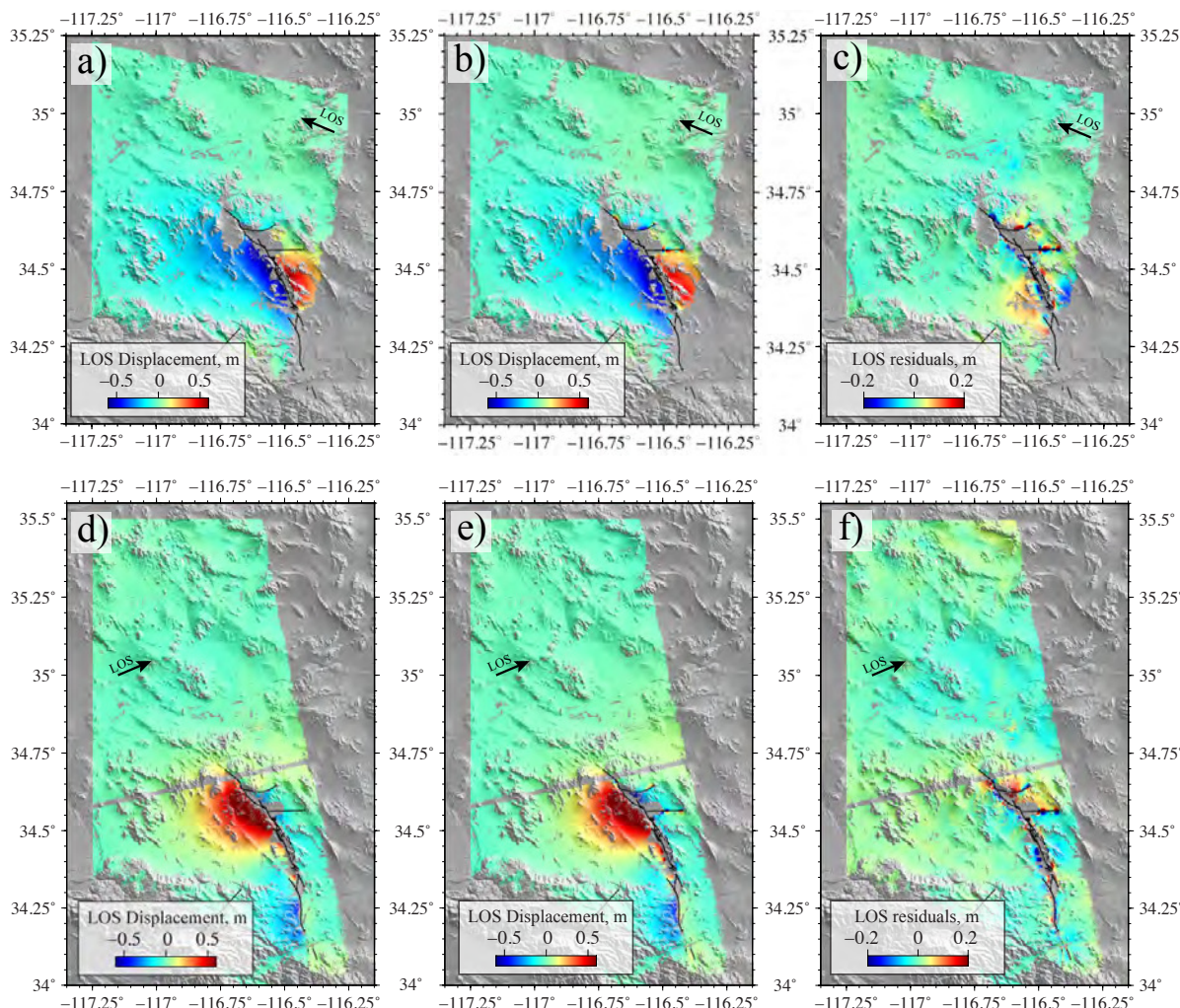
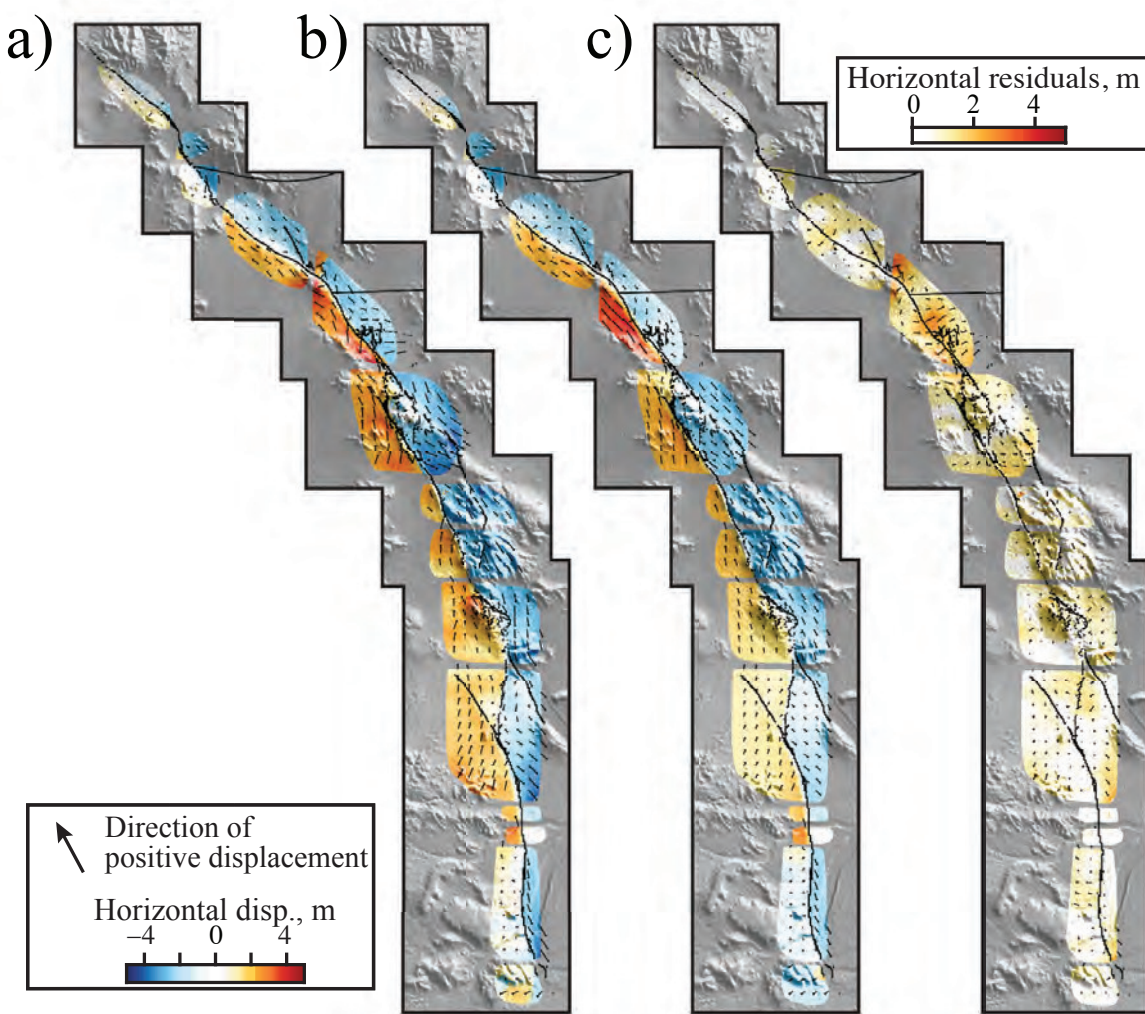


Figure 6. Model performance for InSAR. (a, d) InSAR observations. **(b, e)** Predictions for the posterior mean model. **(c, f)** InSAR residuals of the descending (top) and ascending (bottom) tracks.

1
2
3
4
5
6
7
8
9
10
11
12
13
14
15
16
17
18
19
20
21
22
23
24
25
26
27
28
29
30
31
32
33
34
35
36
37
38
39
40
41
42
43
44
45
46
47
48
49
50
51
52
53
54
55
56
57
58
59
60

34 B. Gombert



38 **Figure 7. Model performance for Optical image correlation data.** (a) Observations. (b) Predictions for
39 the posterior mean model. (c) Residuals. Positive displacements are toward the north-west (see arrow in the
40 legend).
41
42
43
44
45
46
47
48
49
50
51
52
53
54
55
56
57
58
59
60

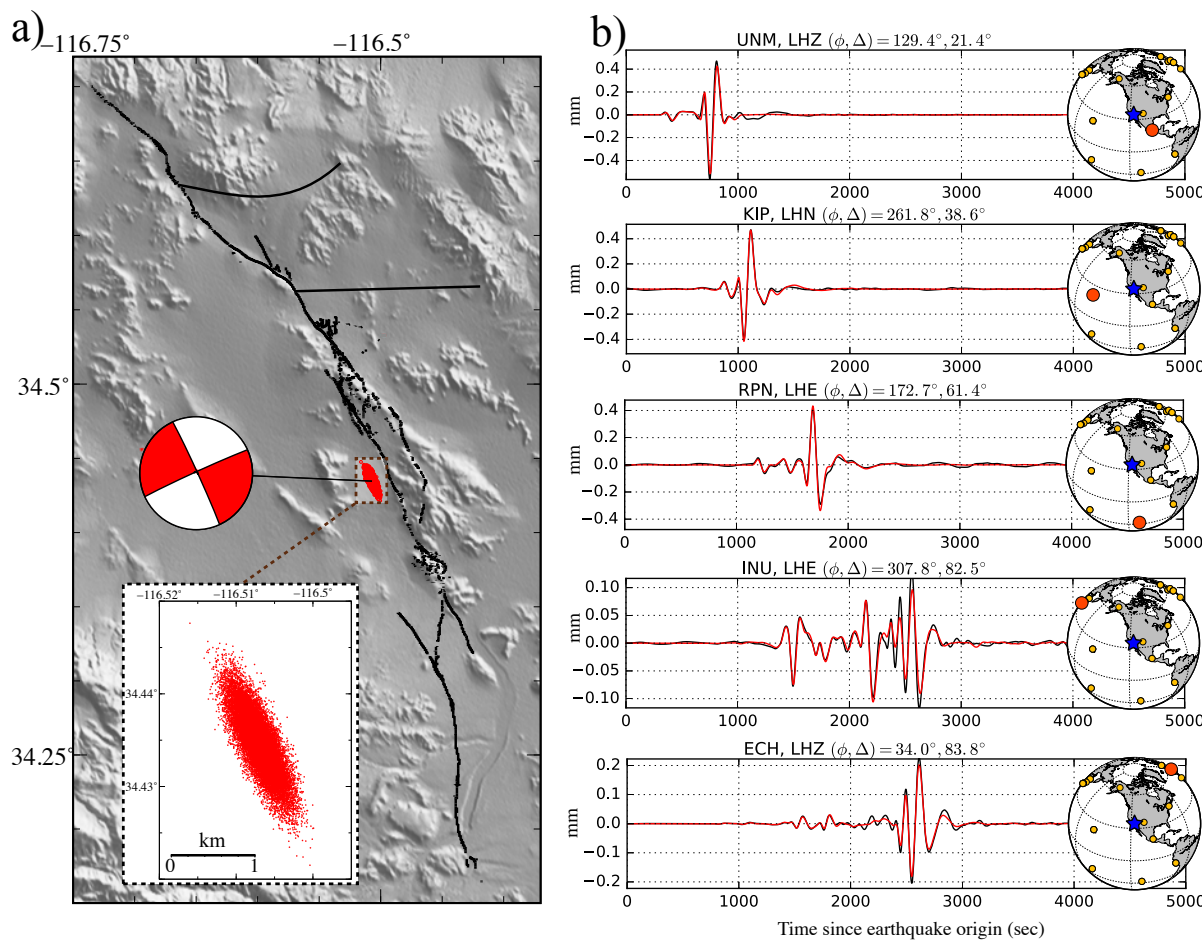


Figure 8. Centroid moment tensor and model validation. (a) Red dots indicate the posterior ensemble of centroid locations derived from our solution. The red focal mechanism is the moment tensor computed from our posterior mean model. (b) Long period observed (black) and predicted (red) synthetic seismograms are plotted for 5 representative stations. The station locations relative to the hypocenter are indicated on the map. The azimuth Φ and epicentral distance Δ is indicated for each station.

1
2
3
4
5
6
7
8
9
10
11
12
13
14
15
16
17
18
19
20
21
22
23
24
25
26
27
28
29
30
31
32
33
34
35
36
37
38
39
40
41
42
43
44
45
46
47
48
49
50
51
52
53
54
55
56
57
58
59
60

36 B. Gombert

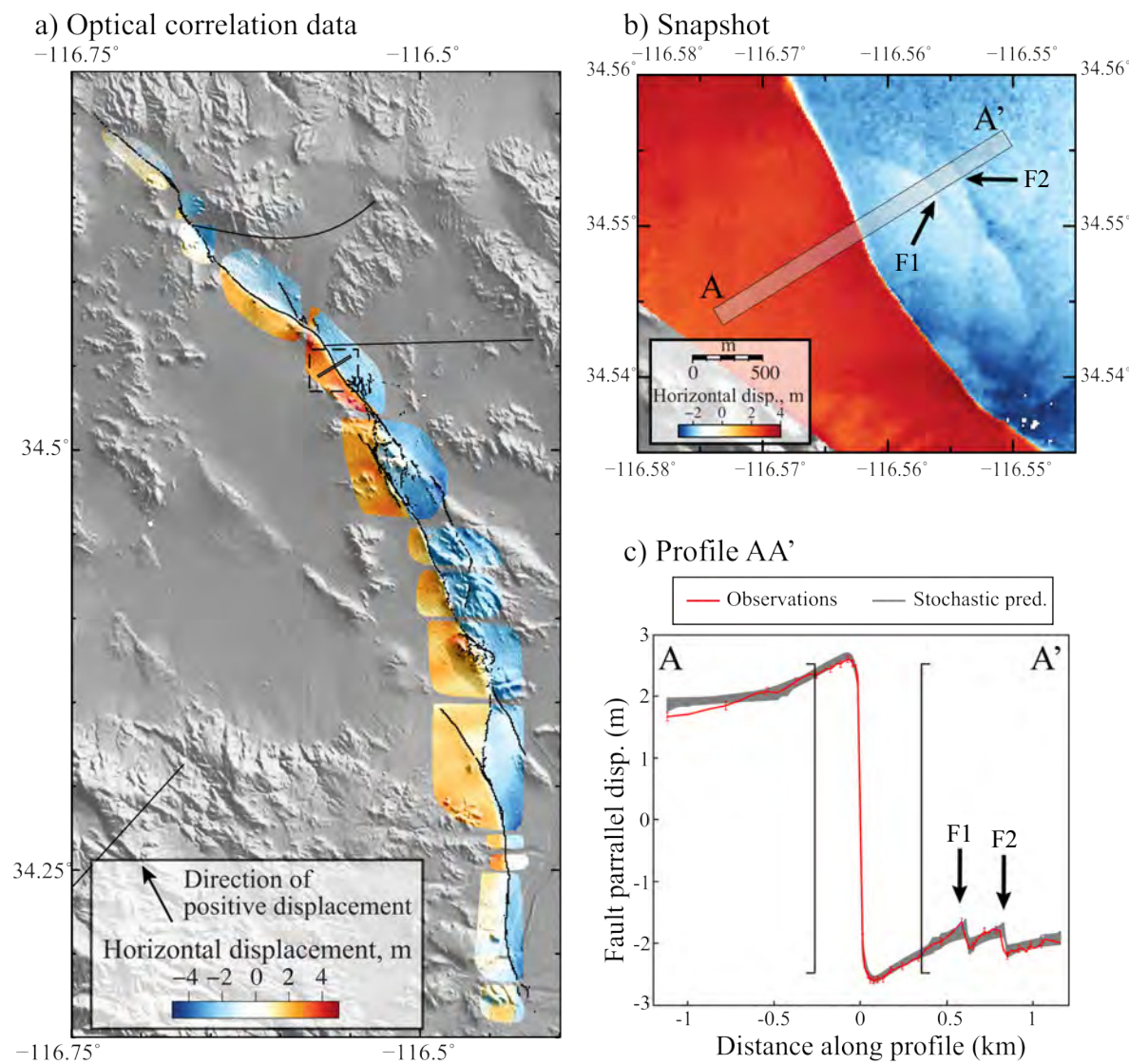


Figure 9. Modeling of Near-field deformation data. (a) Overall view of optical correlation data. The profile shown in (c) is localized with a black line. (b) Close up view of near-field data. Grey rectangle indicate the location of the profile shown in (c). (c) Comparison between observed displacement (in red) and the stochastic predictions (in grey). Black arrows labeled F1 and F2 in (b) and (c) highlight two small secondary ruptures visible in the data. These small ruptures are incorporated in our modeling approach assuming two vertical dislocations. Data inside the black brackets are not used in the inversion of the full 3D slip distribution presented in Fig. 4 to reduce the impact of inelastic effects in the vicinity of the main rupture.

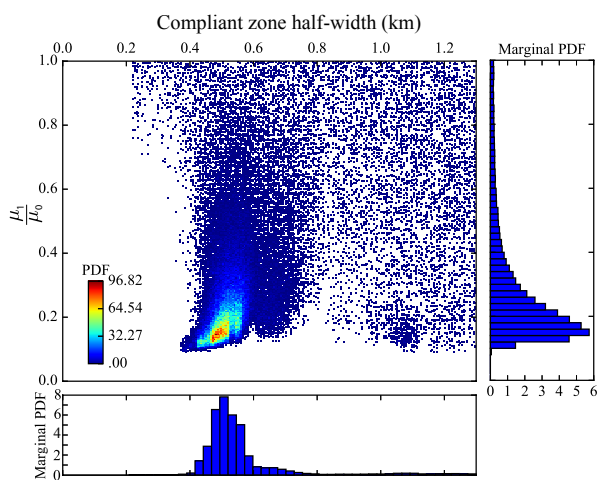
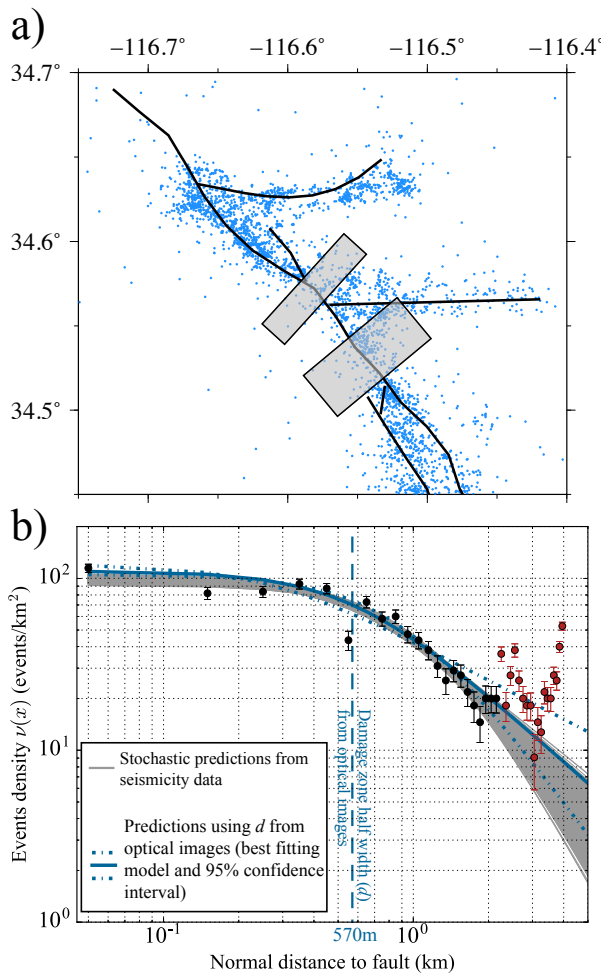


Figure 10. Posterior joint probability distribution of the compliant zone half-width and shear modulus ratio. Dots are model samples that are coloured according to the PDF value. Blue histograms are marginal PDFs for both parameters.

1
2 38 B. Gombert
3
4
5
6
7
8
9
10
11
12
13
14
15
16
17
18
19



36 **Figure 11. Distribution of seismicity across the fault.** (a) Our parametrized fault trace is indicated with
37 thick black lines. Blue dots are aftershock epicenters from Hauksson et al. (2012). Grey rectangles illustrate
38 the location of profiles used for the seismicity density analysis. (b) Seismicity density as a function of fault
39 normal distance. Densities are computed over the two stacked profiles using 100 m wide distance bins.
40 Black circles are resulting event density measurements used in the power-law inversion. Red circles are
41 observations not included in the inversion since they correspond to events located at distance larger than
42 ~2 km that may be partly linked to the southern antithetic fault segment. The 1- σ error bars were obtained
43 by computing the standard deviation of density in each bin from 1000 random catalogs generated according
44 to event location uncertainties.

45
46
47
48
49
50
51
52
53
54
55
56
57
58
59
60

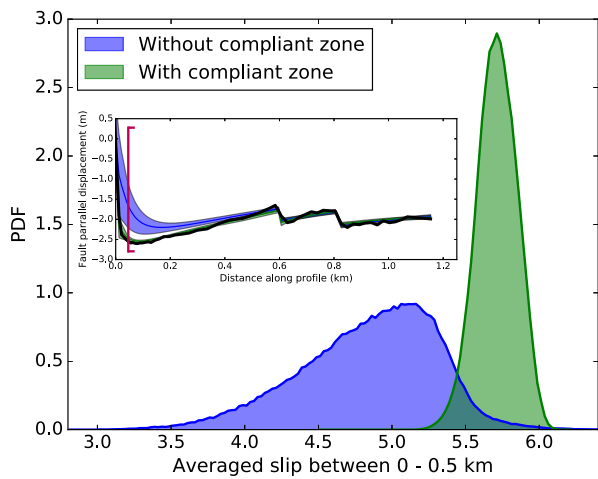


Figure 12. Comparison between shallow slip posterior PDFs assuming an homogeneous half-space (in blue) and accounting for a damage zone of reduced stiffness (in green). The inset shows stochastic predictions for both inversions. Observations are plotted as a thin black line. Blue results are inferred without the data inside the brackets in Fig. 9(c) and green results without the data inside the red brackets at ± 65 m

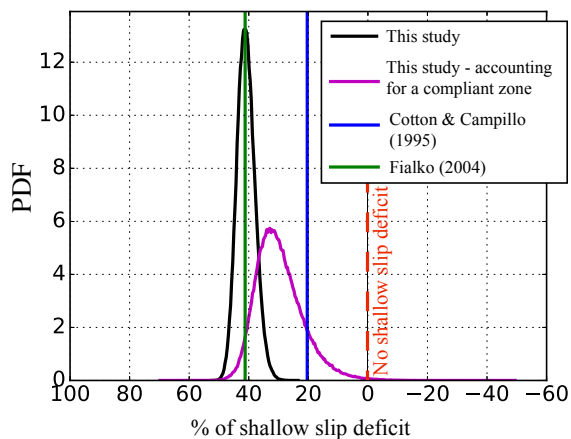


Figure 13. Overall shallow slip deficit (SSD). The black PDF indicate the SSD for the overall rupture presented in Fig. 4. The purple PDF is the SSD corrected from the effect of the damage zone with reduced stiffness. Blue and Green vertical lines are the SSD for two published models (Cotton & Campillo 1995, Fialko 2004b).

1
2
3 Supporting information for the main manuscript
4
5
6

7 Revisiting the 1992 Landers earthquake: a Bayesian exploration of 8 co-seismic slip and off-fault damage 9

10 By
11

12 B. Gombert, Z. Duputel, R. Jolivet, C. Doubre, L. Rivera and M. Simons
13
14

15 *This electronic supplement is a collection of additional figures referenced in the main
16 article. These figures were added to ensure the precision of the description of our
method and results.*
17
18
19
20
21
22

23 Supporting text T1: Modelling errors due to fault parameterization 24 25

26 This study incorporates optical correlation images providing direct measurements of
27 near-fault horizontal displacements (cf., section 2.3 in the main text). Due to the
28 proximity of observation points from the rupture, there can be significant modelling
29 errors due to fault discretization at shallow depth. To limit the impact of such artifacts,
30 we thus remove pixels within 300 m of the fault trace.
31
32

33 To quantify the remaining modelling errors due to fault parameterization, we compare
34 the deformation field predicted assuming a finely discretized fault (with 300 m-long
35 patches) to a coarser fault geometry (with 1.5 km long patches as used in this study).
36 This test is presented in Figure 9b for the southern portion of the Emerson fault where
37 we observe large slip of ~4.1 m at shallow depth. Comparing the results for the loose
38 and fine geometries (Figure S2), we observe a maximum modelling error of 23 cm due
39 to the use of a simplified fault geometry. The mean modelling error is ~8 cm. These
40 values being directly proportional to fault slip, they can be considered as upper bounds
41 since we consider a region of large slip (more than twice the average shallow slip over
42 the entire rupture). In addition, these errors fall within the observations uncertainties
43 (which are ~42 cm on this image) and represent only 6% of the data amplitude.
44
45
46
47
48
49
50
51
52
53
54
55
56
57
58
59
60

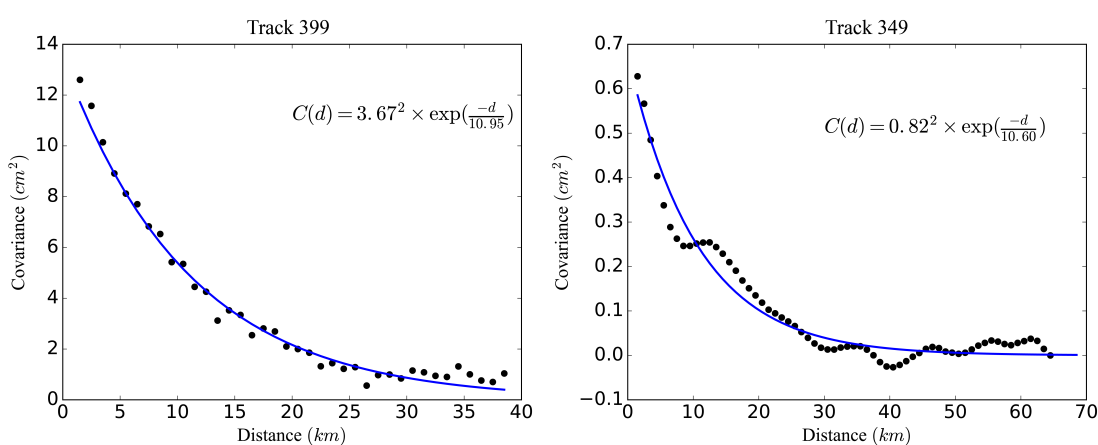


Figure S1: Empirical covariance functions for the InSAR observations: 1D empirical covariance functions and the associated best-fit exponential function for the descending (left) and ascending (right) tracks. For each image, we compute the empirical covariance as a function of the distance between pixels and then fit an exponential function to these covariances (Jolivet et al., 2012). This exponential function is then used to build the data covariance matrix used in the inversion.

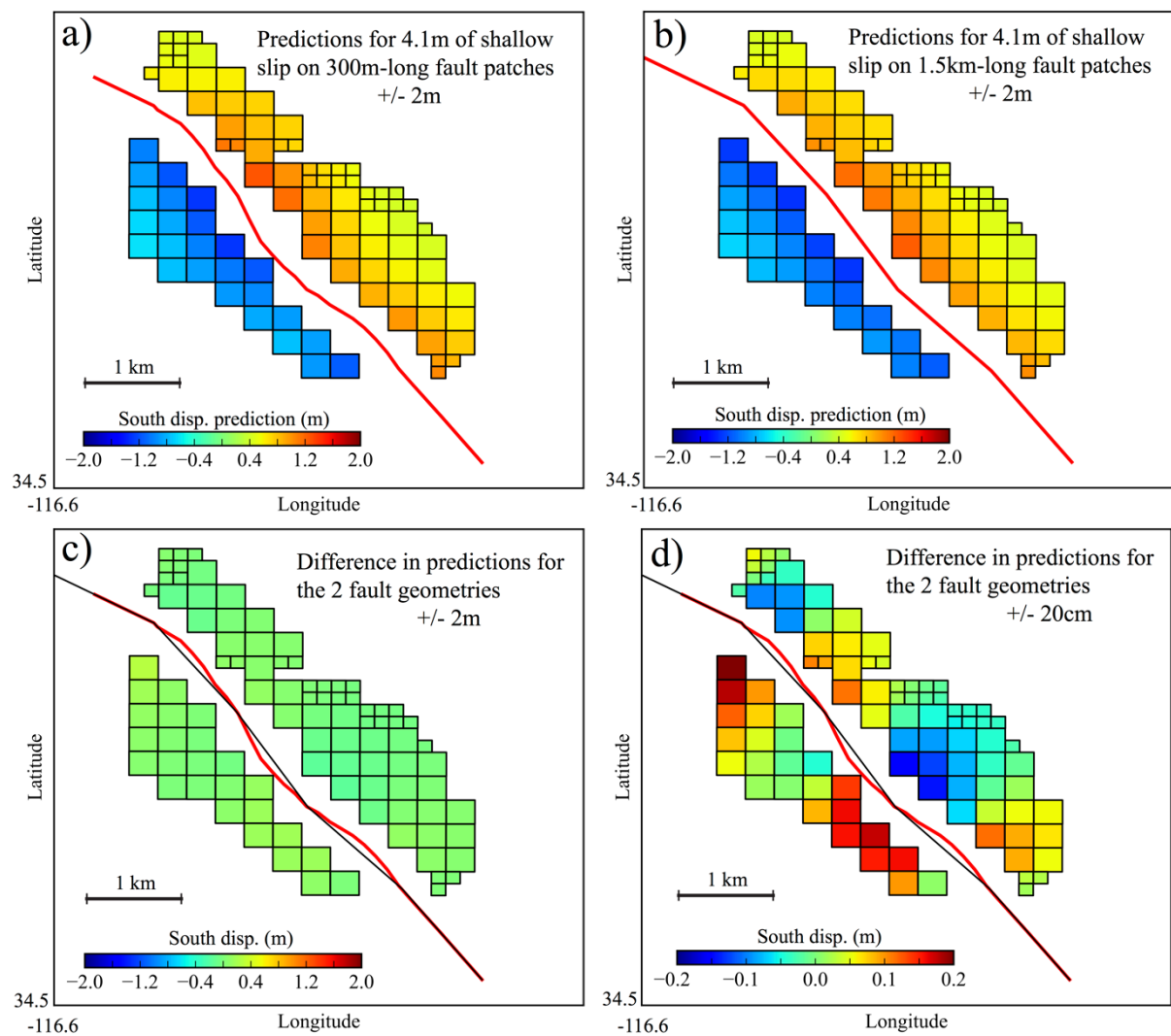
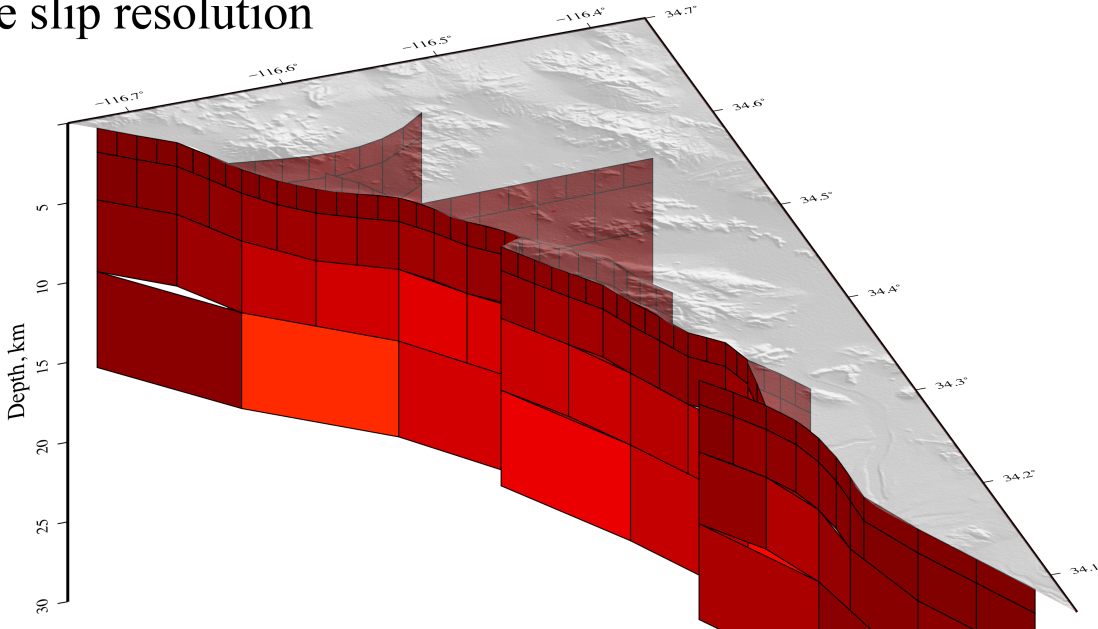
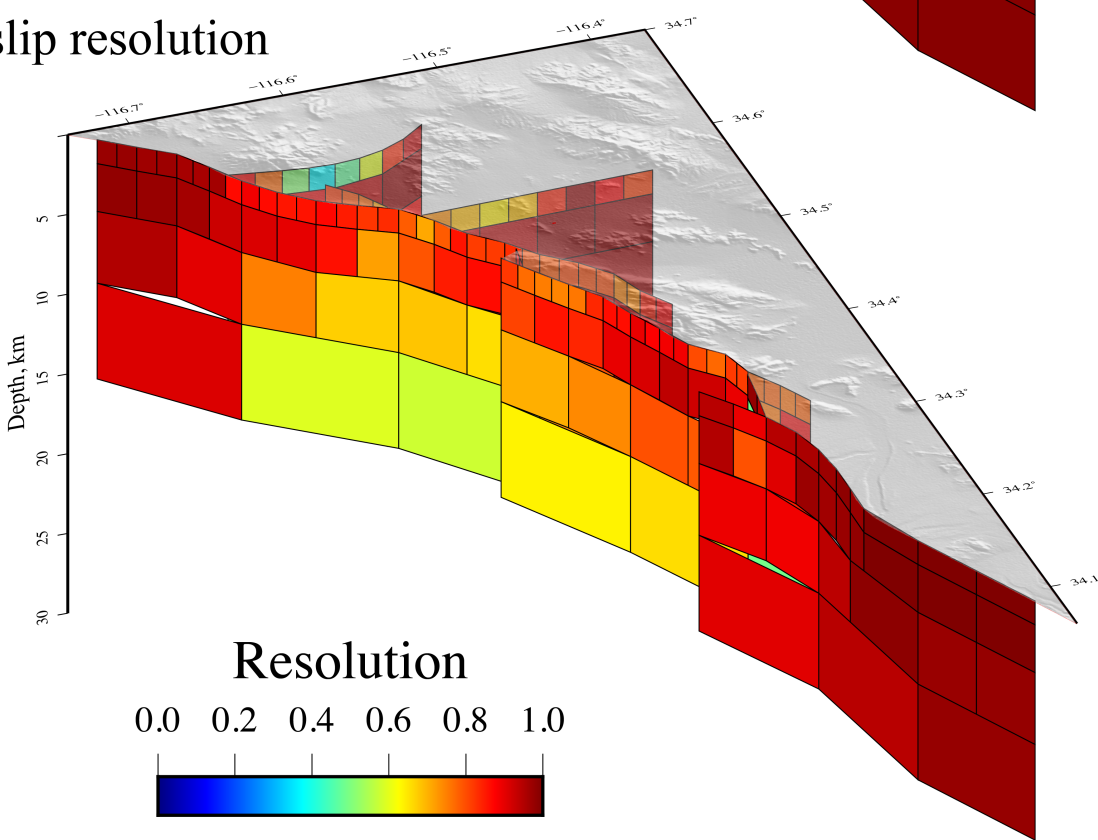


Figure S2: Effect of geometry on forward modelling. **(a)** Forward model predictions for the one of the optical images mosaic imposing 4.1m of slip on a shallow fault with 300m long patches. **(b)** same as (a) but with a broader geometry (1.5km-long patches). **(c)** and **(d)** Difference between (a) and (b).

1
2
3
4 Strike slip resolution



27 Dip slip resolution



54 **Figure S3:** Problem resolution. For each slip component, we compute the Resolution
55 matrix as $R = C_m G^T (G C_m G^T + C_\chi)^{-1} G$. The diagonal values are plotted on the fault.
56 The closer to 1, the better is the resolution of the parameter.

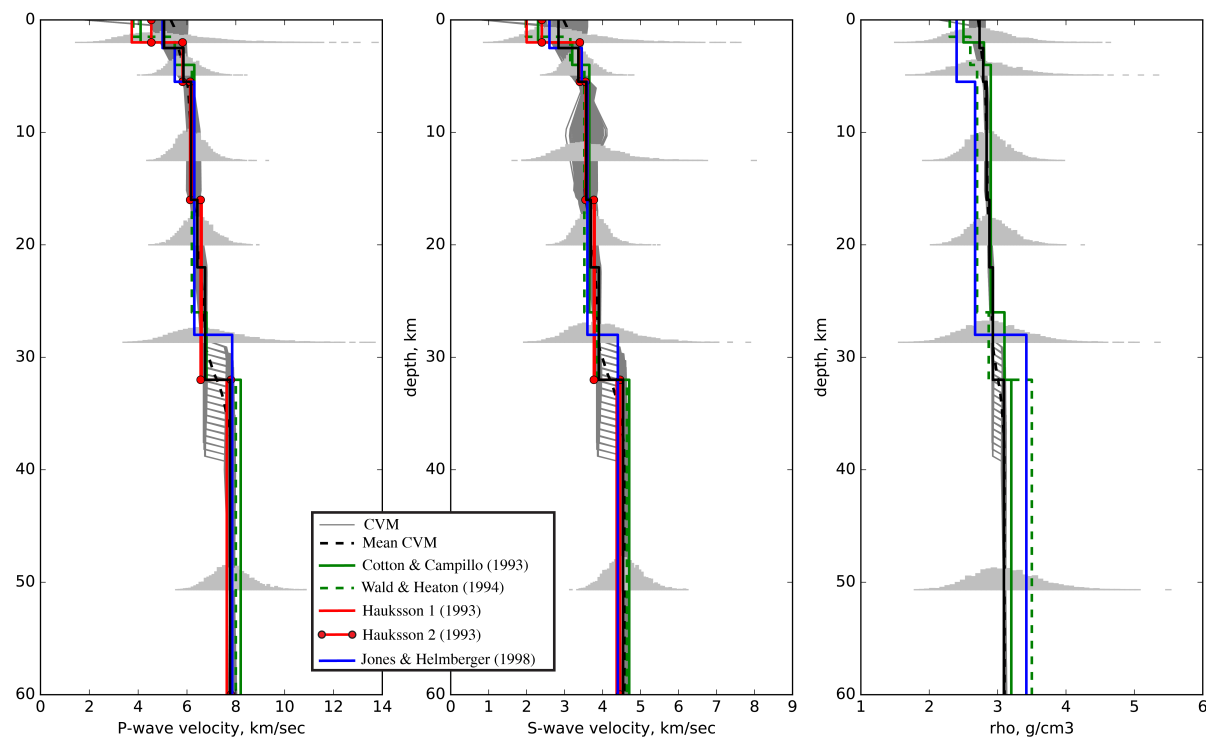


Figure S4: Different models variability of the P-wave, S-wave, and density as a function of depth in the Landers area. Grey lines are model values of the 3D Community Velocity Model (CVM, Kohler et al. 2003) available at <http://scedc.caltech.edu/research-tools/3d-velocity.html> (last accessed January 2016). The dashed black line represents the averaged CVM value for this area. A layered version used in this study for Green's function [GF] calculations is plotted as a solid black line. Models from Cotton and Campillo (1993), Wald and Heaton (1994), Hauksson (1993), and Jones and Helmberger (1998) are plotted as solid green, dashed green, red, and blue lines, respectively. Grey histograms are the probability density function representing our confidence level on the elastic properties, as used to build the model prediction error. Histograms are derived from the averaged CVM assuming a Gaussian distribution.

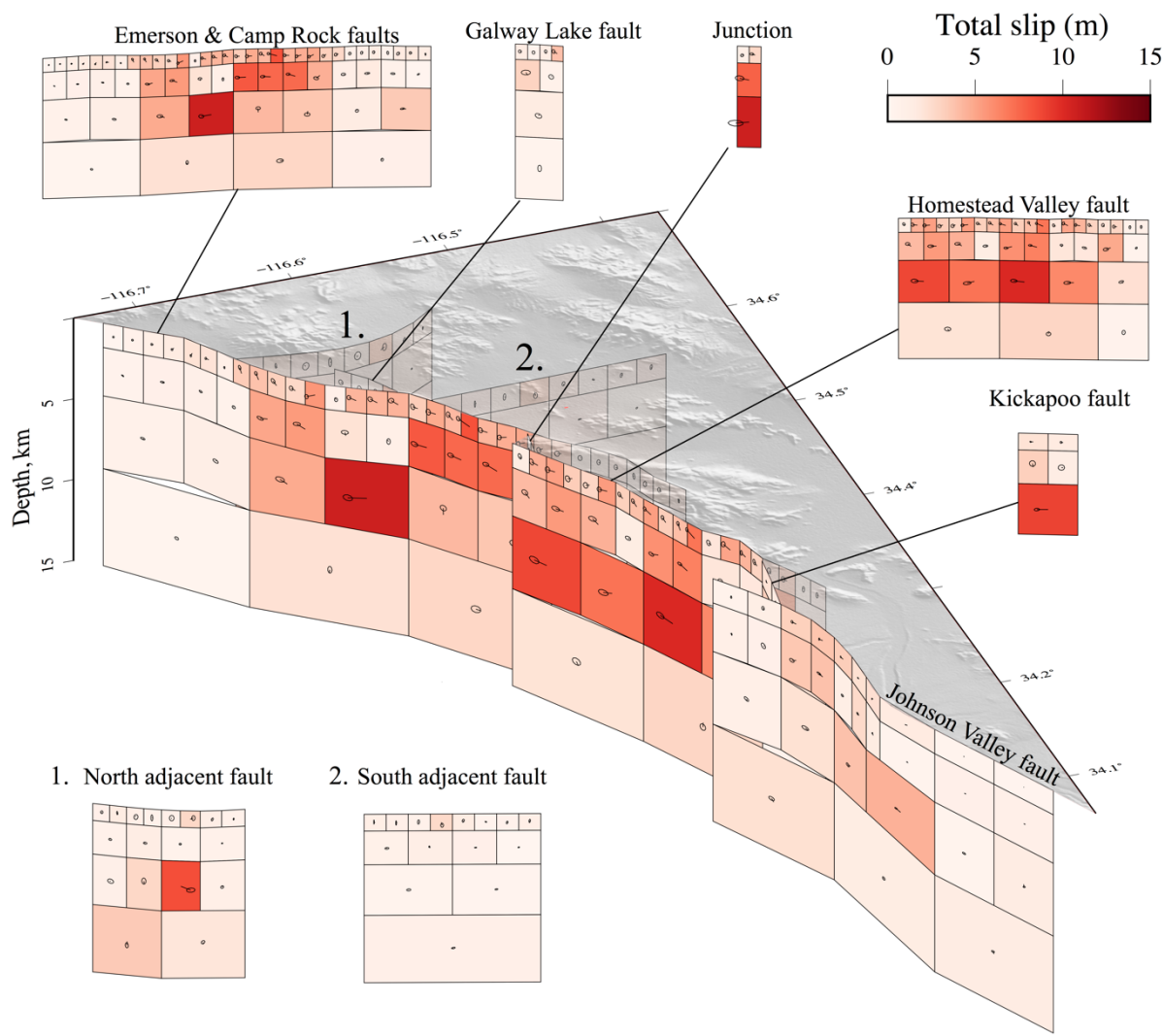


Figure S5: Posterior mean co-seismic slip model. The color of each subfault patch indicates the slip amplitude. Arrows and their associated 95% confidence ellipse indicate the slip direction and uncertainty.

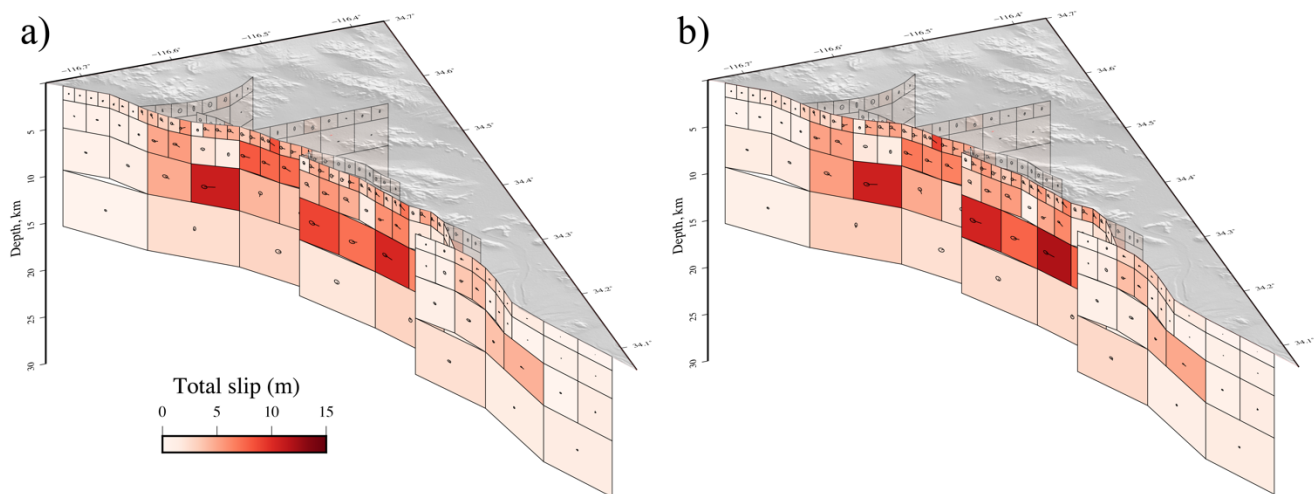


Figure S6: (a) Posterior mode coseismic slip models. It is built by considering the maximum of each marginal PDF. (b) Posterior maximum model (“best-fitting” model). The colour of each subfault patch indicates the slip amplitude. Arrows and their associated 95% confidence ellipse indicate the slip direction and uncertainty.

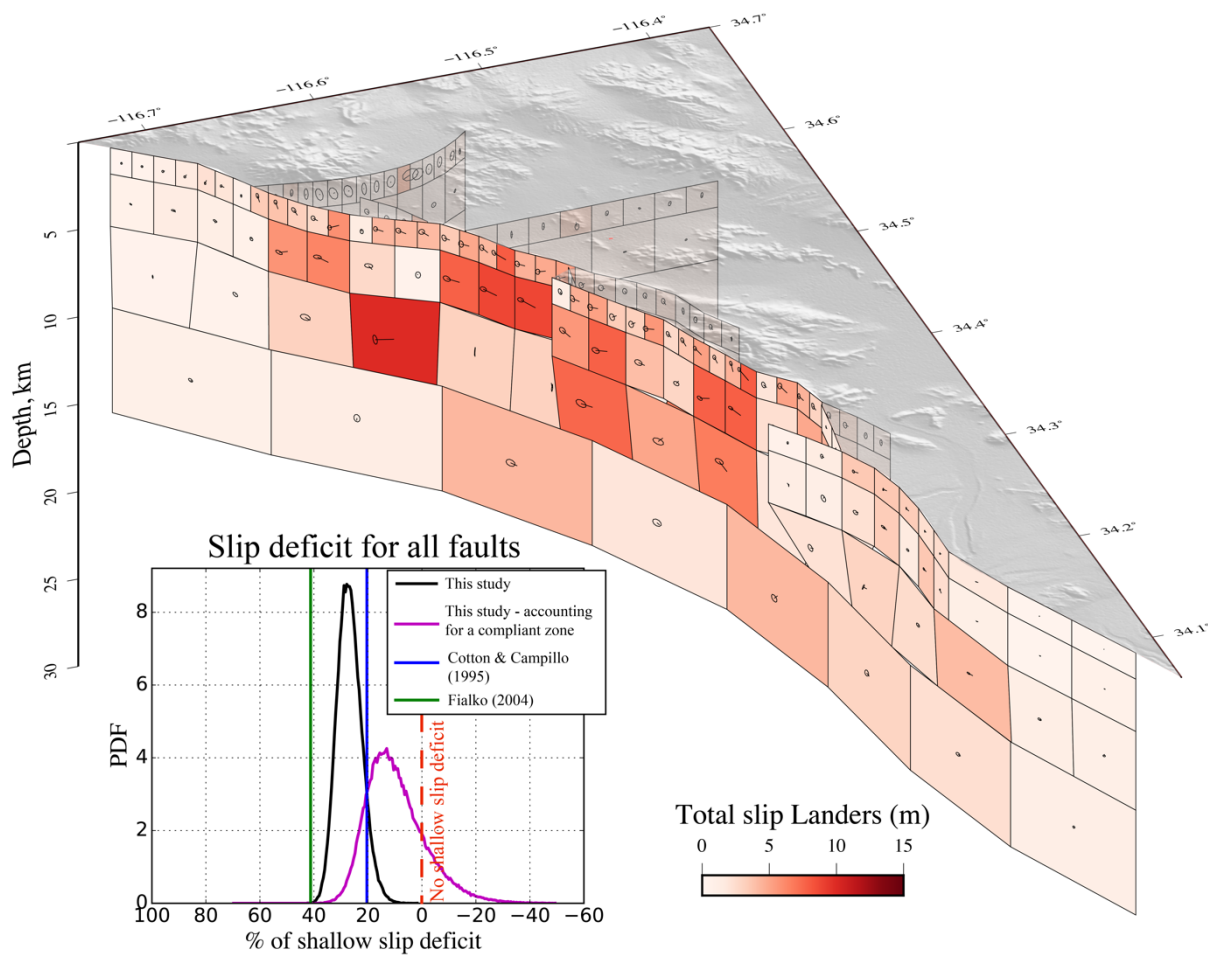


Figure S7: Posterior mean coseismic slip models for an alternative “flower” geometry. The colour of each subfault patch indicates the slip amplitude. Arrows and their associated 95% confidence ellipse indicate the slip direction and uncertainty. At the bottom are shown the results for the segments numbered from 1 to 5. We show the PDF of SSD as a black line on the bottom-right insert. The magenta line illustrates the SSD value when corrected from a compliant zone. On the same plots are represented the SSD for two published models, Cotton and Campillo (1995) and Fialko (2004).

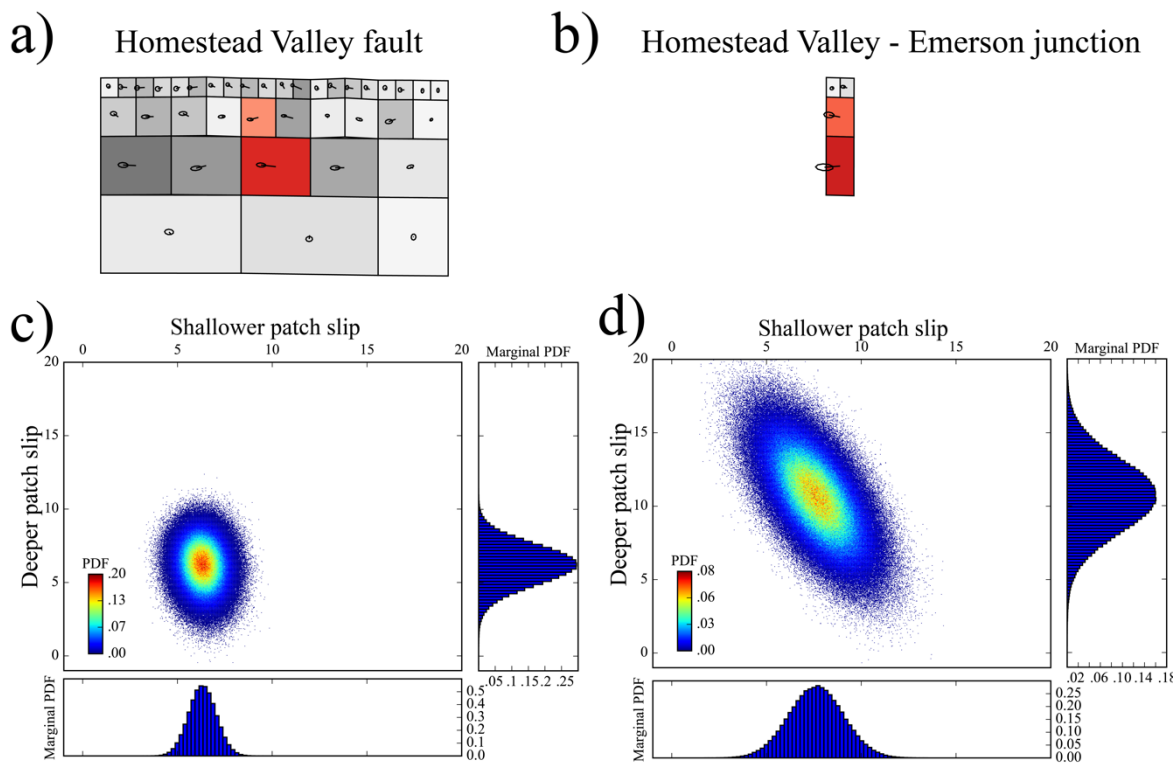


Figure S8: Posterior covariance of two along-dip patches of the Homestead Valley segment and the Homestead Valley – Camp Rock segments junction. **(a)** Homestead Valley and **(b)** Homestead Valley – Camp Rock junction posterior mean coseismic slip. Correlation is computed for the two coloured patches. **(c)** and **(d)** Joint posterior PDF of the strike-slip of two contiguous patches along-dip. Dots are model samples that are coloured according to the PDF value. Blue histograms are marginal PDFs for both parameters.

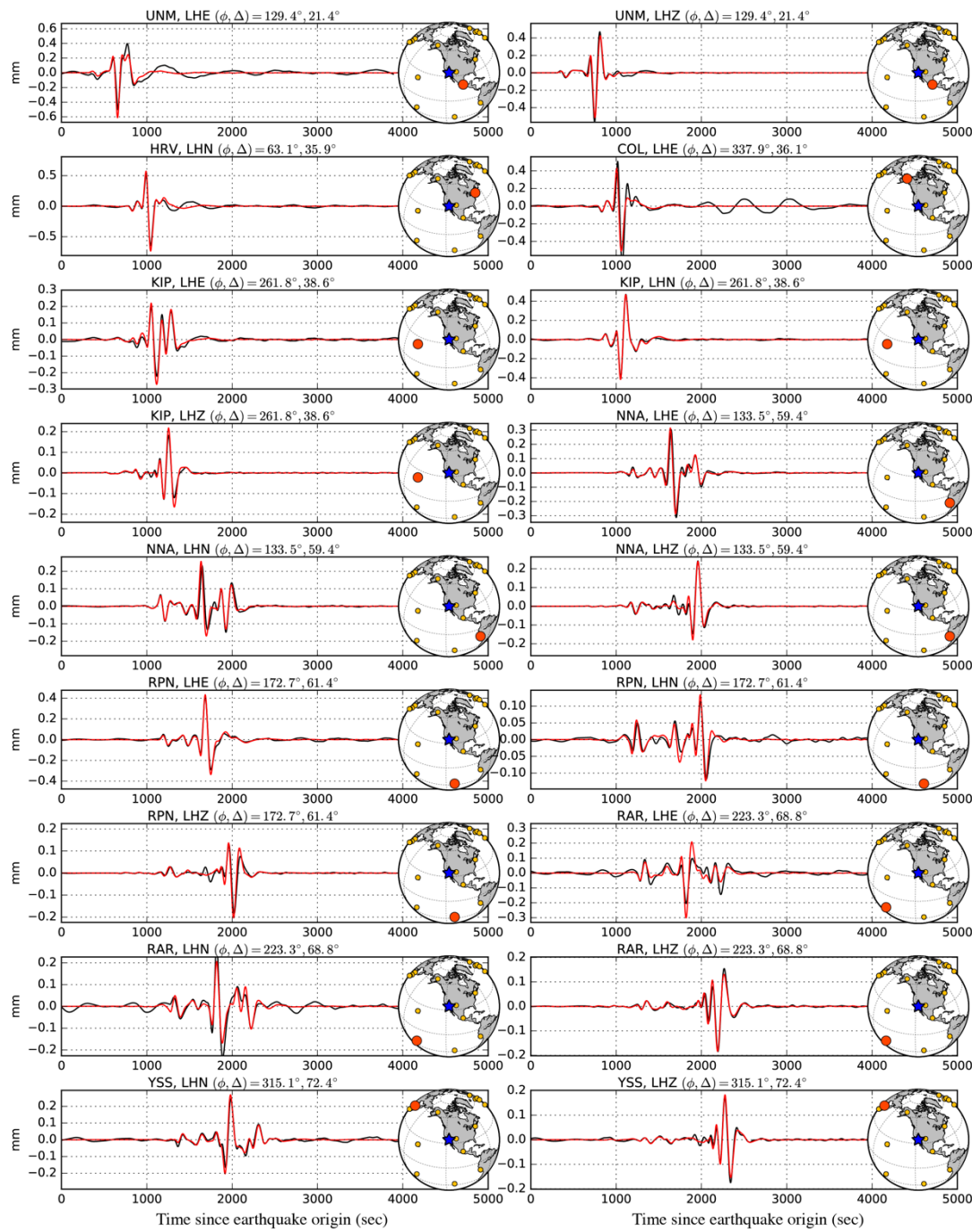


Figure S9: Broadband seismograms (black line) and synthetics computed from the posterior mean model moment tensor (red line) are plotted for 5 stations along with their locations. On each map, the blue star and the red dot indicate the hypocenter and station locations, respectively. For each trace is indicated the station azimuth ϕ and epicentral distance Δ .

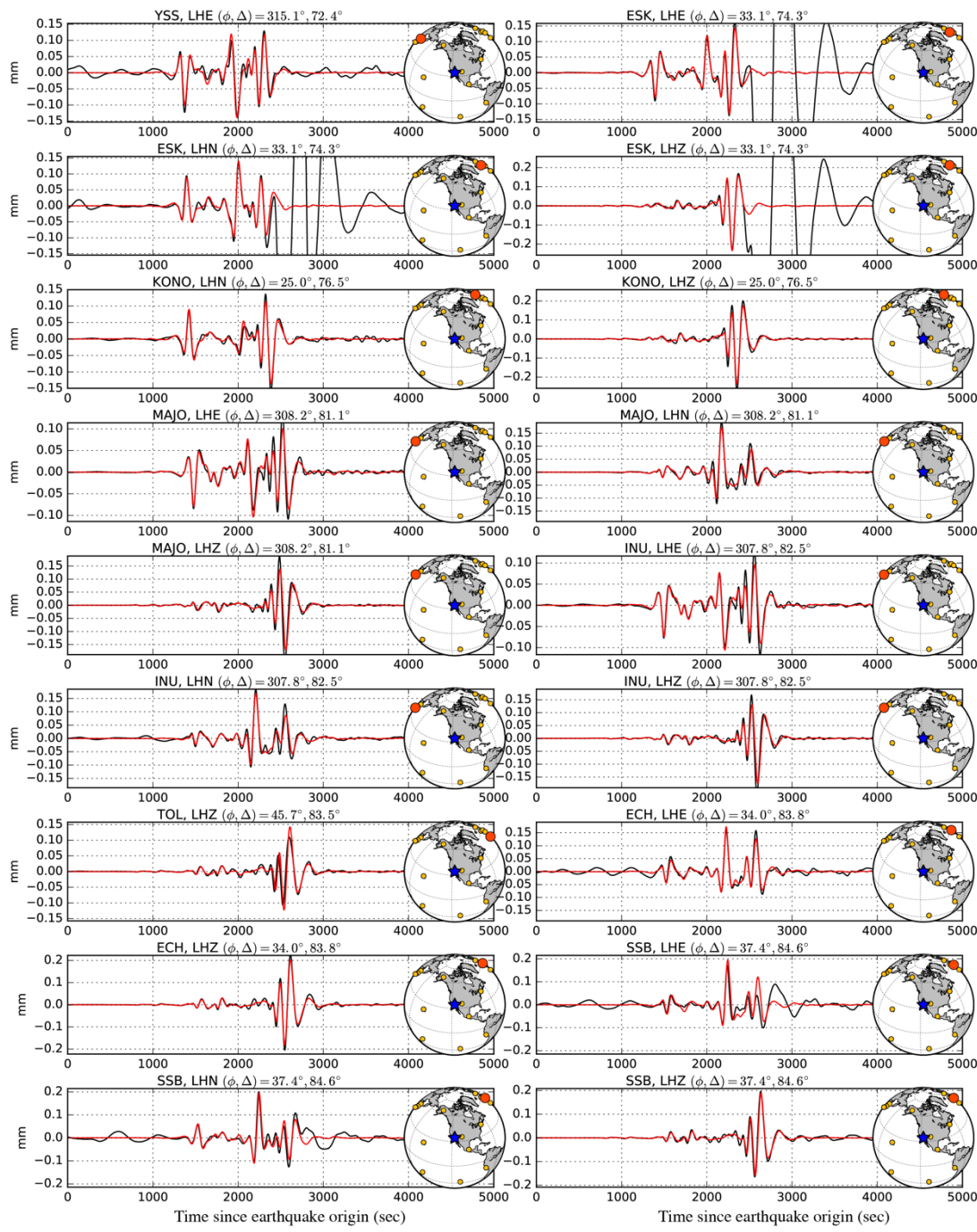


Figure S10: Figure S9 continued. Broadband seismograms (black line) and synthetics computed from the posterior mean model moment tensor (red line) are plotted for 5 stations along with their locations. On each map, the blue star and the red dot indicate the hypocenter and station locations, respectively. For each trace is indicated the station azimuth ϕ and epicentral distance Δ .

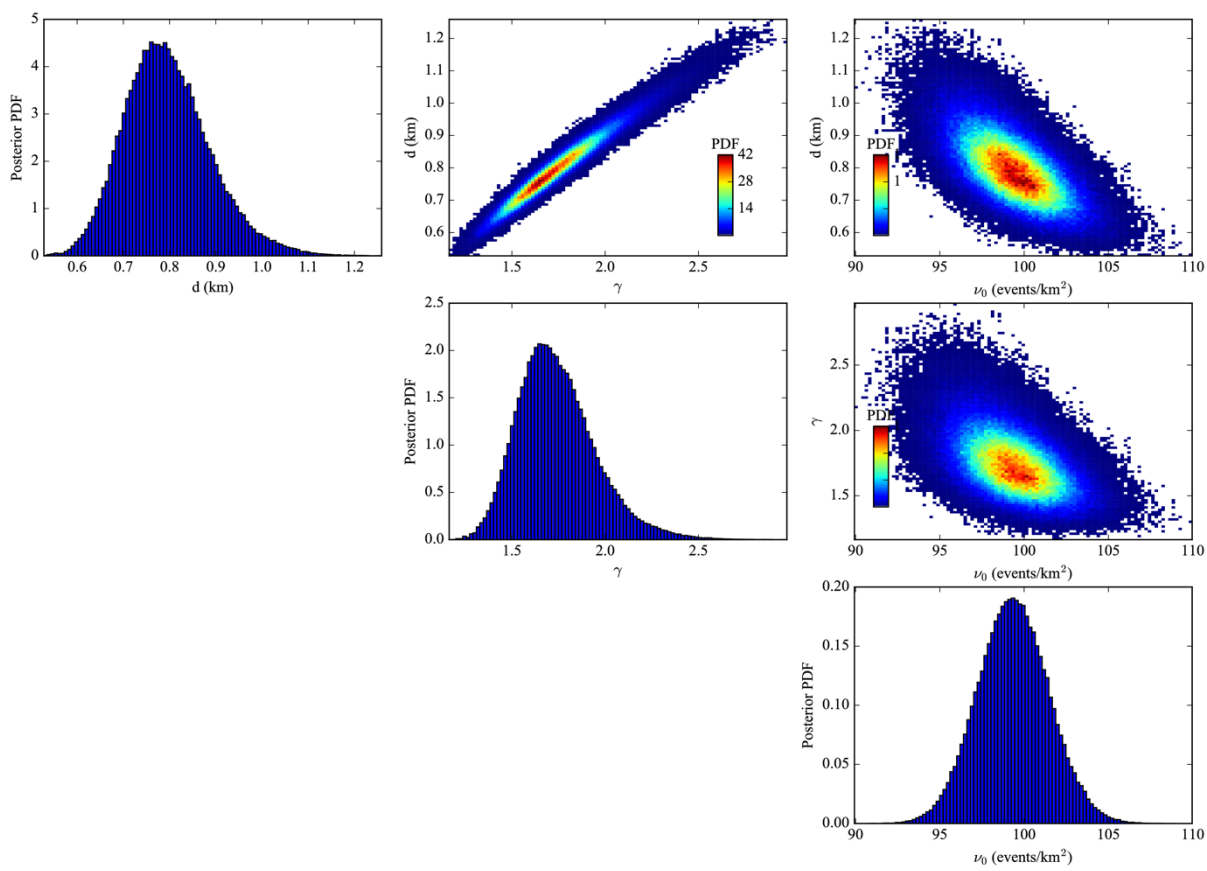


Figure S11: Results of the Metropolis sampling of the aftershock density profile parameters ν_0 , d and γ . 1D plots are posterior marginal PDFs and 2D plots are posterior joint PDFs. On the 2D histograms dots are model samples that are coloured according to the PDF value. Hot colours indicate region of high-probability.

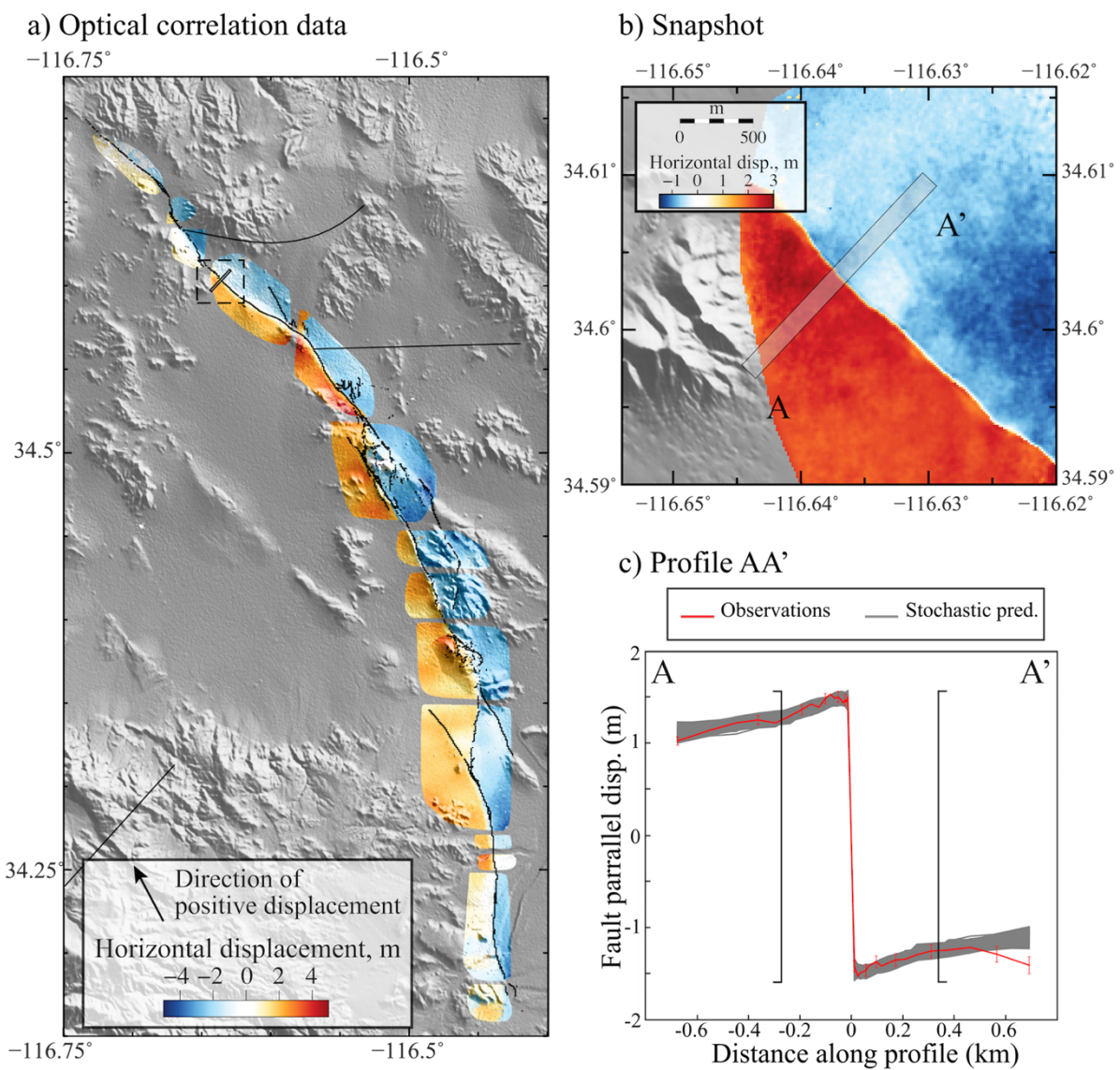


Figure S12: Modeling of Near-field deformation data. **(a)** Localization of the profiles in the optical correlation observations. **(b)** Close up view of near-field data. Grey rectangle indicate the location of the inverted profile. **(c)** Comparison between observed displacement (in red) and the stochastic predictions (in grey). Data inside the black brackets are not used in the inversion of the full 3D slip distribution presented in Figure 6 of the main manuscript.

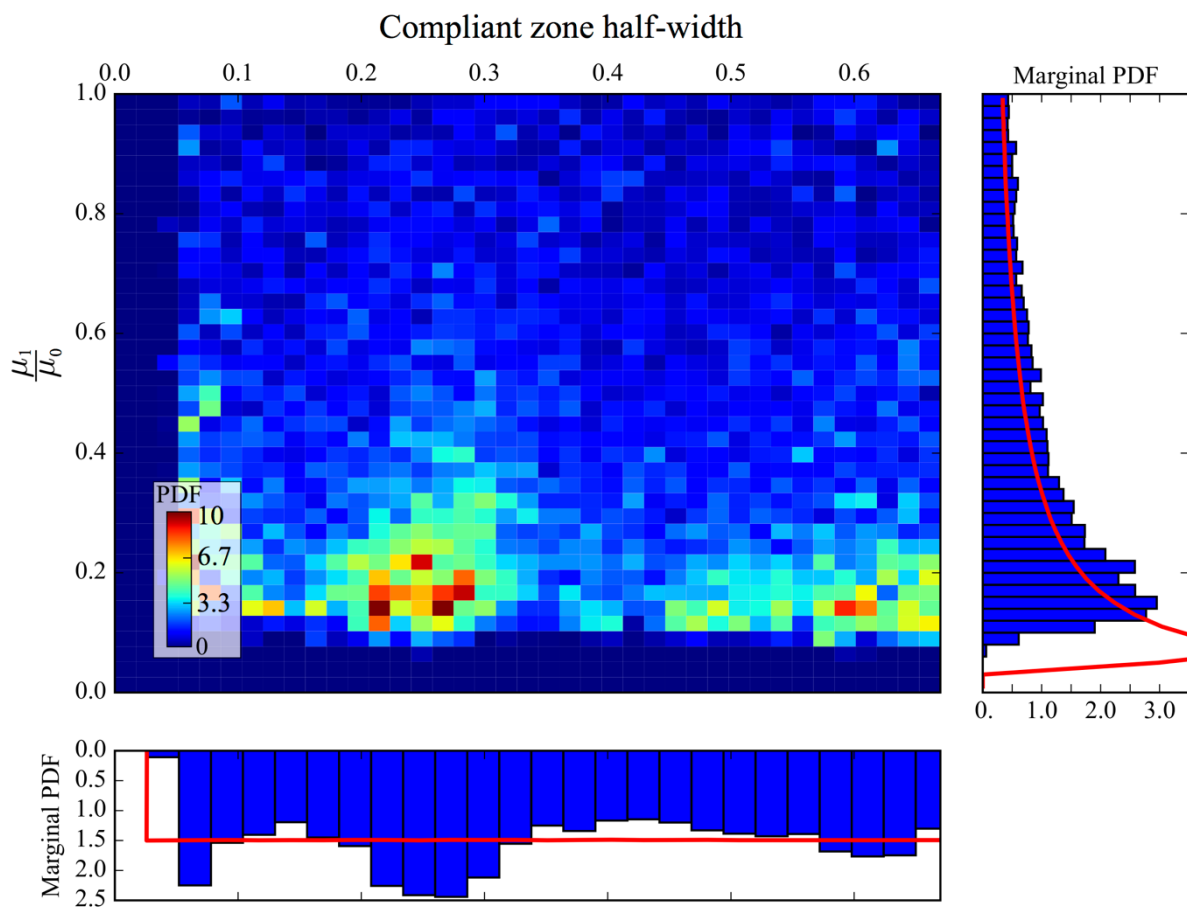


Figure S13: Posterior joint probability distribution of the compliant zone half-width and shear modulus ratio for the profile presented in Figure S12. Dots are model samples that are coloured according to the PDF value. Blue histograms are marginal PDFs for both parameters. Red lines are the prior information used in the sampling.

References

- Cotton, F., Campillo, M., 1995. Frequency domain inversion of strong motions: Application to the 1992 Landers earthquake. *Journal of Geophysical Research* 100, 3961. doi:10.1029/94JB02121
- Duputel, Z., Agram, P.S., Simons, M., Minson, S.E., Beck, J.L., 2014. Accounting for prediction uncertainty when inferring subsurface fault slip. *Geophysical Journal International* 197, 464–482. doi:10.1093/gji/ggt517
- Fialko, Y., 2004. Probing the mechanical properties of seismically active crust with space geodesy: Study of the coseismic deformation due to the 1992 M_w 7.3 Landers (southern California) earthquake. *Journal of Geophysical Research* 109. doi:10.1029/2003JB002756
- Hauksson, E., Jones, L.M., Hutton, K., Eberhart-Phillips, D., 1993. The 1992 Landers Earthquake Sequence: Seismological observations. *Journal of Geophysical Research* 98, 19835. doi:10.1029/93JB02384
- Jolivet, R., Lasserre, C., Doin, M.-P., Guillou, S., Peltzer, G., Dailu, R., Sun, J., Shen, Z.-K., Xu, X., 2012. Shallow creep on the Haiyuan Fault (Gansu, China) revealed by SAR Interferometry: CREEP ON THE HAIYUAN FAULT. *Journal of Geophysical Research: Solid Earth* 117, n/a-n/a. doi:10.1029/2011JB008732
- Jones, L.E., Helmberger, D.V., 1998. Earthquake source parameters and fault kinematics in the eastern California shear zone. *Bulletin of the Seismological Society of America* 88, 1337–1352.
- Kohler, M.D., 2003. Mantle Heterogeneities and the SCEC Reference Three-Dimensional Seismic Velocity Model Version 3. *Bulletin of the Seismological Society of America* 93, 757–774. doi:10.1785/0120020017
- Wald, D.J., Heaton, T.H., 1994. Spatial and temporal distribution of slip for the 1992 Landers, California, earthquake. *Bulletin of the Seismological Society of America* 84, 668–691.